# Interannual Variations in the Intraseasonal Variability of Spring Precipitation over Southern China and the Possible Mechanisms

ZIXUAN ZENG[a,b] AND JIANQI SUN[a,b]

[a] *Nansen-Zhu International Research Center, Institute of Atmospheric Physics, Chinese Academy of Sciences, Beijing, China*
[b] *College of Earth and Planetary Sciences, University of Chinese Academy of Sciences, Beijing, China*

(Manuscript received 19 November 2022, in final form 9 March 2023, accepted 4 April 2023)

ABSTRACT: This study first investigates the interannual variations in spring precipitation intraseasonal variability over southern China (SC). The results show that SC spring precipitation exhibits distinct intraseasonal variations with a period of 7–25 days. The first mode of 7–25-day precipitation intraseasonal variability (PIV) displays a monopole pattern over SC, and the PIV magnitude is largely determined by the upward motion intensity during intraseasonal precipitation events. Further analysis suggests that two atmospheric wave trains are observed during intraseasonal precipitation events, which propagate eastward from the North Atlantic along the northern and southern paths. In strong PIV years, the two wave trains can propagate to East Asia and show coordinated influences. The resultant low pressure to the west of SC causes strong upward motion and PIV over SC by bringing strong zonal vorticity and meridional temperature advection. In weak PIV years, the southern wave train can only propagate to the Bay of Bengal; therefore, the northern wave train plays a major role. The resultant low pressure is now over the upper to middle reaches of the Yangtze River, which causes relatively weak upward motion and PIV over SC by bringing weak meridional vorticity and temperature advection. Further analysis indicates that the sea surface temperature (SST) condition over the tropical Indian Ocean and the South China Sea is essential for southern wave train propagation. The warming SST over the regions can intensify westerlies to its north and consequently favors the propagation of the southern wave train to SC, eventually contributing to strong PIV over SC.

KEYWORDS: Atmosphere; Asia; Precipitation; Spring season; Interannual variability; Intraseasonal variability

## 1. Introduction

Southern China (SC) is an important agricultural base in China. Spring is the first persistent rainy season after the dry winter, and anomalous precipitation during this period can exert a great influence on agricultural activities in SC and other regions (LinHo et al. 2008; W. Li et al. 2016; Lu et al. 2020; Zhu et al. 2023). In addition, SC has the largest precipitation amount in spring over China, with a magnitude approximately equal to that of summer precipitation, and the variations of precipitation are directly related to droughts and floods over the region (Yang and Lau 2004; Wu and Mao 2016; Wu et al. 2023). Therefore, improving the understanding of spring precipitation variations in SC is of significance.

Previous studies have investigated the variations in spring precipitation over SC mainly from the seasonal mean perspective. They indicated that the interannual variations in SC spring precipitation could be influenced by various atmospheric circulations. Among them, the western North Pacific anticyclone (WNPA) is regarded as a key one affecting SC precipitation (Jiang and Zhao 2012; Z. Li et al. 2016; You and Jia 2018; Lu et al. 2023; Yang et al. 2023). Generally, an intensified WNPA would lead to increased spring precipitation over SC by inducing anomalous southwesterlies and associated moisture transport to the region (Wu and Mao 2016; Zeng and Sun 2023). Additionally, the East Asia subtropical jet (EASJ) is another important atmospheric factor affecting SC spring precipitation, and the enhanced EASJ favors increased spring precipitation over SC by modulating the local upward motion over the region (Huang et al. 2015; Wu et al. 2015; Gu et al. 2021). In addition to the above two, other atmospheric circulations, such as the Hadley cell (Qiang and Yang 2013) and North Atlantic Oscillation/Arctic Oscillation (Qu et al. 2017; Han and Zhang 2022), could also exert influences on SC spring precipitation. In addition to atmospheric circulations, some boundary factors have also been revealed to have great impacts on the interannual variations in spring precipitation over SC, including tropical Pacific sea surface temperature (SST) anomalies (Feng and Li 2011; Cheng et al. 2018; Gu et al. 2018; Park et al. 2020), Indian Ocean SST anomalies (Feng et al. 2014; Yuan et al. 2019), North Atlantic SST anomalies (You and Jia 2018), Eurasian snow cover (Jia et al. 2018; Zhang and Sun 2021), and Arctic sea ice (Wu et al. 2016; Zhang et al. 2022). In addition to seasonal mean precipitation, Lin et al. (2022) documented that the SST cooling in the equatorial western Pacific favors persistent and heavy precipitation in the first rainy season of SC by causing a strong western Pacific subtropical high.

In addition, spring precipitation over SC also exhibits significant decadal change. For example, Xin et al. (2006) revealed that late-spring precipitation to the south of the Yangtze River has undergone a remarkable decrease since the late 1970s, and upper-troposphere cooling over central China resulting from the decadal change in the preceding winter North Atlantic Oscillation plays a key role. Zhu et al. (2014) suggested that there is a marked decadal decrease in spring precipitation over SC around the mid-1990s, which could be attributed to enhanced

*Corresponding author*: Jianqi Sun, sunjq@mail.iap.ac.cn

DOI: 10.1175/JCLI-D-22-0863.1

© 2023 American Meteorological Society. This published article is licensed under the terms of the default AMS reuse license. For information regarding reuse of this content and general copyright information, consult the AMS Copyright Policy (www.ametsoc.org/PUBSReuseLicenses).

Brought to you by INSTITUTE OF ATMOSPHERIC PHYSICS, CAS | Unauthenticated | Downloaded 07/13/23 02:29 PM UTC

convection over the Maritime Continent associated with decadal warming in the western Pacific and cooling in the eastern Pacific. In addition, Zeng and Sun (2022) reported a significant decadal increase in spring extreme consecutive dry days over the middle and lower reaches of the Yangtze River around the early 2000s, in which both the intensified Mongolian high and weakened WNPA show a combined contribution. Additionally, the relationship between SC precipitation and boundary forcings could also exhibit a decadal change (Ren et al. 2017; Wang et al. 2019). For example, Wang et al. (2019) indicated that the impact of preceding summer warm-pool ocean heat content on SC spring precipitation experienced a remarkable decadal weakening around 1983.

In addition to interannual and interdecadal variations, intraseasonal variations could also be observed in spring precipitation over SC (Pan et al. 2013; Tan and Wang 2016). The influence of intraseasonal atmospheric patterns on spring precipitation over SC, especially the first rainy season precipitation over South China, is emphasized by some previous studies (Zhang et al. 2011; Li et al. 2014; W. Li et al. 2016; Miao et al. 2019; Jiang et al. 2020; Liu et al. 2023). For instance, Miao et al. (2019) documented that persistent heavy rainfall events during the first rainy season over South China could be influenced by two low-frequency wave trains in the mid–high latitudes and the tropical low-frequency oscillation of convection over the South China Sea. Tan and Wang (2016) also suggested that the northward-propagated Rossby wave triggered by convection over the eastern Indian Ocean–Indonesia and southeastward-propagated geopotential height anomalies from the high latitudes of Europe–western Siberia have a superposition effect on the low-frequency variation in April–June precipitation in Jiangnan. Liu et al. (2023) recently suggested that the majority of presummer extreme precipitation events in South China were formed under the combined influences of intraseasonal and synoptic-scale signals.

The aforementioned studies have improved our understanding of spring precipitation variations over SC from the intraseasonal time scale. Intraseasonal variability could also exhibit distinct interannual variations (Li et al. 2015; Deng and Li 2016; Qi et al. 2019; Nie and Sun 2022), and the interannual variations in intraseasonal variability could affect the forecast on intraseasonal and seasonal time scales (Lin et al. 2016). Therefore, it is of great importance to investigate the interannual variations in intraseasonal variability. However, the features and related mechanisms for the interannual variations in spring precipitation intraseasonal variability (PIV) over SC are still unclear. Therefore, this study attempts to first derive the dominant mode of interannual variations in spring PIV over SC and then explore the associated atmospheric circulations and boundary forcings.

The remainder of this paper is organized as follows: The data and analysis methods are introduced in section 2. The interannual variations in spring PIV over SC are shown in section 3. Section 4 investigates the possible reasons for the strong and weak PIV. Finally, a summary and discussion are given in section 5.

## 2. Data and methods

### a. Data

Daily observed precipitation data at 699 stations in China during 1961–2019 are used to analyze the intraseasonal variations in spring precipitation, which are provided by the National Meteorological Information Centre of the China Meteorological Administration (http://data.cma.cn). The data were subjected to quality control before release, including climatological and regional limit value check, temporal and spatial consistency check, and artificial check; and the correctness rate of these data is nearly 100% (Ren et al. 2015). Following the method of a previous study (Sun and Ao 2013), we removed the stations with missing data for more than 10% of days in a given year or 1% of total days in all years. The missing daily records are filled by the interpolated values of the surrounding stations, based on the Cressman method (Cressman 1959). In addition, the CN05.1 daily dataset is also employed to verify the results, which is on a 0.25° × 0.25° grid over the Chinese mainland and is derived by the interpolation of climate anomalies from more than 2400 observing stations (Wu and Gao 2013)

The daily atmospheric reanalysis dataset is derived from the Japanese 55-year Reanalysis Project (JRA-55), which is on a 1.25° × 1.25° grid and has been available since 1958 (Kobayashi et al. 2015). Variables including horizontal winds, vertical velocity, specific humidity, surface pressure, surface temperature, air temperature, and geopotential height are analyzed here. The monthly SST dataset is from the Hadley Centre Sea Ice and Sea Surface Temperature dataset, version 1 (HadISST1; Rayner et al. 2003), which is on a 1° × 1° grid and has been available since 1870.

### b. Methods

Similar to Cheng et al. (2020), the process to extract the intraseasonal components of variables is as follows. First, the annual cycle (mean and first three harmonics of climatological annual variation) is removed. Second, a 5-day running mean is calculated to remove the synoptic components. Third, the intraseasonal anomalies are extracted by applying a Lanczos bandpass filter with a specified period range (Duchon 1979). Additionally, spectral analysis can decompose the total energy of time series into components at different frequencies (Wei 2007), which is performed to diagnose the major periods of precipitation series.

The moisture budget equation is used to investigate the possible mechanisms responsible for intraseasonal precipitation anomalies in this study. The specific formula, with reference to Seager and Henderson (2013), is expressed as follows:

$$\mathrm{PR}' - E' = -\left\|\frac{\partial q}{\partial t}\right\|' - \|\mathbf{V}\cdot\nabla q\|' - \left\|\omega\frac{\partial q}{\partial P}\right\|',$$

where prime means the intraseasonal anomaly of the variable; $\|X\|$ denotes the vertical integral from surface pressure to 300 hPa, that is, $\|X\| = 1/g\int_{300}^{P_s} X\,dP$; PR − $E$ is the precipitation minus surface evaporation; $\mathbf{V} = (u, v)$ denotes the horizontal wind; and $q$, $\omega$, and $P$ are the specific humidity, vertical

Brought to you by INSTITUTE OF ATMOSPHERIC PHYSICS, CAS | Unauthenticated | Downloaded 07/13/23 02:29 PM UTC

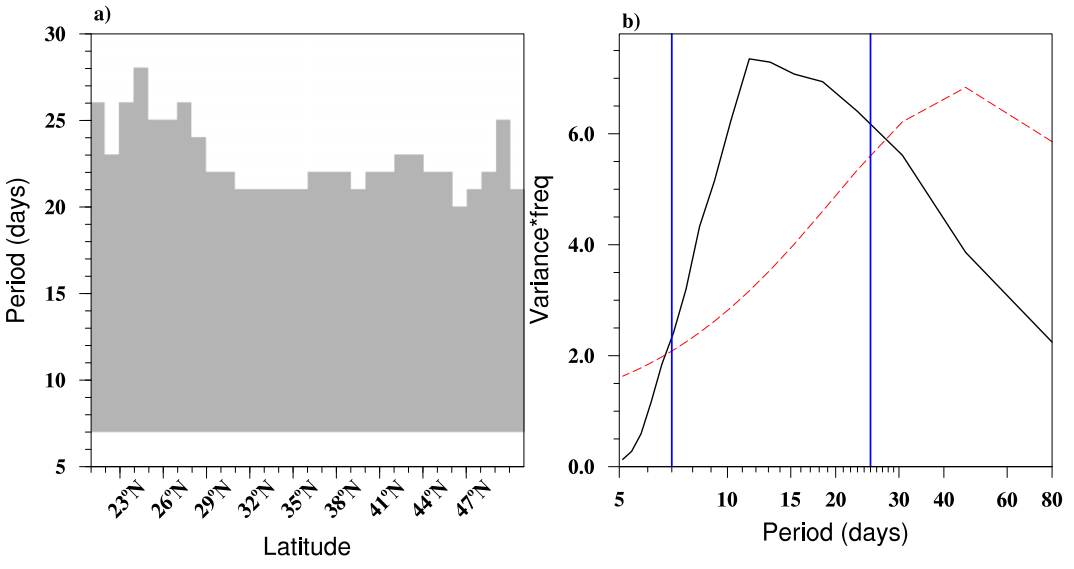


FIG. 1. (a) Significant periods of spring daily-precipitation series averaged over the 30 subregions (east of 110°E and one latitudinal interval from 21°N northward to 51°N) during 1961–2019 based on spectrum analysis. Gray shading denotes the 95% confidence level, and the horizontal axis indicates the latitude of subregions. (b) Multiyear mean power spectrum (black line) of spring daily precipitation averaged over the region east of 110°E and between 21° and 29°N during 1961–2019. The red line indicates the 95% confidence level. The daily precipitation series are obtained by removing the annual cycle and synoptic components.

velocity, and pressure, respectively. Specifically, the three terms on the right of the moisture equation represent the local change in specific humidity, horizontal moisture advection, and vertical moisture advection. Here, evaporation is a relatively small term, which is not discussed in this study.

The wave activity flux (**WAF**) is used to investigate the propagation of stationary Rossby waves. The horizontal component of the **WAF** is calculated based on the method of Takaya and Nakamura (2001), as follows:

$$\mathbf{WAF} = \frac{P_{1000}}{2|\overline{\mathbf{V}}|}\begin{bmatrix} \overline{u}(\psi_x'^2 - \psi'\psi_{xx}') + \overline{v}(\psi_x'\psi_y' - \psi'\psi_{xy}') \\ \overline{u}(\psi_x'\psi_y' - \psi'\psi_{xy}') + \overline{v}(\psi_y'^2 - \psi'\psi_{yy}') \end{bmatrix},$$

where $\psi$ is the streamfunction, the prime signifies the intraseasonal perturbation, the subscript indicates the partial derivative, $\overline{\mathbf{V}} = (\overline{u}, \overline{v})$ denotes the climatological spring-mean horizontal wind, and $P_{1000}$ represents pressure scaled by 1000 hPa.

To analyze the influences of atmospheric circulations on precipitation intraseasonal variations, the quasigeostrophic omega equation without diabatic heating in pressure coordinates is diagnosed based on the following formula (Holton 1992):

$$\left(\sigma\nabla^2 + f^2\frac{\partial^2}{\partial P^2}\right)\omega' = \left\langle f\frac{\partial}{\partial P}[\mathbf{V}\cdot\boldsymbol{\nabla}(f+\zeta)]\right\rangle' + \left\langle \nabla^2\left[\frac{R}{P}\mathbf{V}\cdot\boldsymbol{\nabla}T\right]\right\rangle',$$

where $f$ is the Coriolis parameter, $\sigma$ is the static stability, $\zeta$ is the relative vorticity, $R$ is the dry air gas constant, $T$ is the air temperature, $\nabla^2$ is the horizontal Laplacian operator, and $\boldsymbol{\nabla}$ is the horizontal del operator. The prime means intraseasonal component. The term on the left-hand side is proportional to $-\omega'$, and the two terms on the right-hand side denote the vertical difference in horizontal vorticity advection (dynamic term) and horizontal temperature advection (thermal term). Each term of the two could be further divided into zonal and meridional components.

To quantitatively compare the relative contributions of different time scales, an individual variable $X$ could be separated into the low-frequency background state component $\overline{X}$, intraseasonal component $X'$, and synoptic-scale component $X''$ (Hsu et al. 2011), that is, $X = \overline{X} + X' + X''$.

In this study, the spring is March–May. The statistical methods adopted include empirical orthogonal function (EOF), composite, regression, and correlation. The Student's $t$ test was employed for the statistical significance test. In addition, the Theil–Sen trend estimation method was used to calculate the linear trend, and the nonparametric Mann–Kendall test is used to test the significance.

## 3. Interannual variations in spring PIV over SC

To investigate the interannual variations in spring PIV over SC, it is necessary to objectively identify the key region first. To do so, we divide eastern China (east of 110°E) into 30 subregions with one latitudinal interval from 21°N northward to 51°N and then conduct power spectral analysis for the spring precipitation averaged over the 30 subregions. Here, the annual cycle and synoptic components are first removed from the daily precipitation series. As shown in Fig. 1a, spring precipitation in most subregions in SC displays similar significant periods, exhibiting periodic oscillations of approximately 7–25 days; in contrast, spring precipitation at most subregions

Brought to you by INSTITUTE OF ATMOSPHERIC PHYSICS, CAS | Unauthenticated | Downloaded 07/13/23 02:29 PM UTC

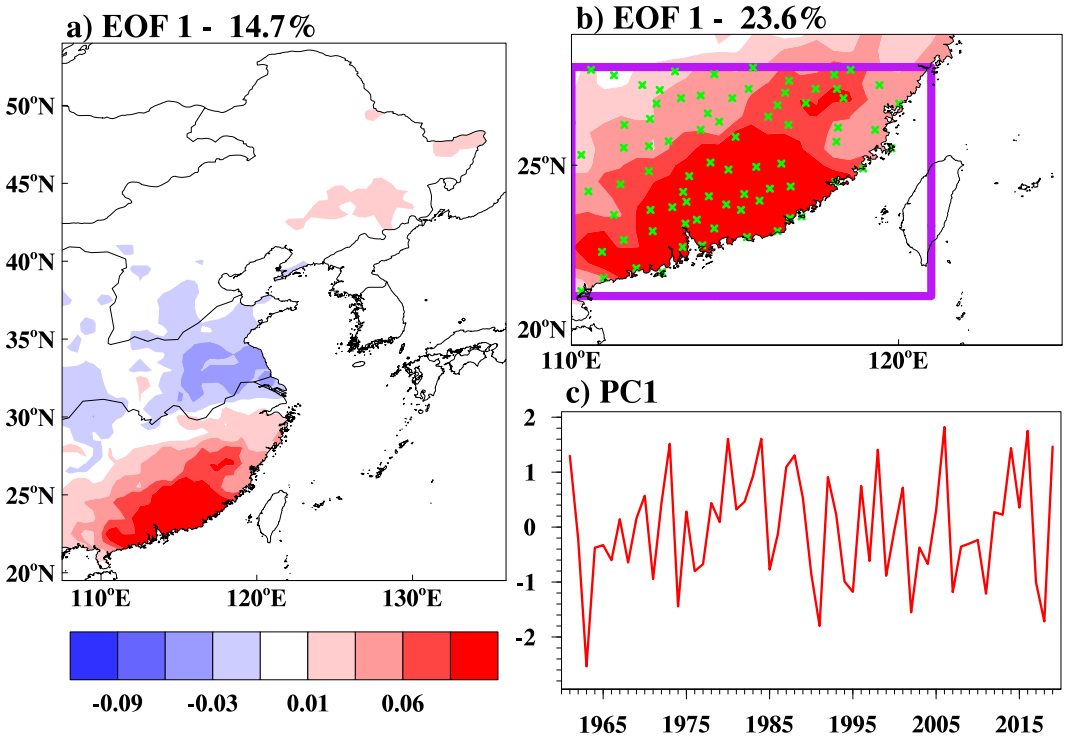


FIG. 2. (a) The first EOF mode of the standard deviation of 7–25-day filtered daily precipitation in spring at stations over China east of 107.5°E during 1961–2019. (b) The first EOF mode and (c) corresponding normalized PC1 of the standard deviation of 7–25-day filtered daily precipitation in spring at stations over China east of 110°E and between 21° and 29°N during 1961–2019. Shading is interpolated from the station loading based on the Cressman method. The box in (b) denotes the SC domain, and the crosses are observation stations.

north of the Yangtze River displays a relatively smaller significant period range. Therefore, the region east of 110°E and between 21° and 29°N is first chosen to determine the dominant periods of spring precipitation intraseasonal variations over SC. Figure 1b gives the power spectrum of the daily precipitation averaged over the above-selected region, which suggests that there is a significant 7–25-day period in precipitation anomalies, with the outstanding period around 10–15 days. Such a significant period is also basically consistent with that of previous studies on spring intraseasonal precipitation over SC, also known as the quasi-biweekly oscillation (Pan et al. 2013; Miao et al. 2019). Therefore, in the following analysis, the 7–25-day precipitation variability is used to denote the PIV over SC.

Then, 7–25-day Lanczos bandpass filtering is applied to derive the intraseasonal component of daily precipitation, and the standard deviation of the 7–25-day filtered daily precipitation in each spring is used to reflect the interannual variations in PIV over SC. To derive the dominant mode of interannual variations of the spring PIV over SC, the EOF analysis is first performed to the standard deviation of 7–25-day filtered daily precipitation in spring at stations over China east of 107.5°E during 1961–2019. The first mode has a variance contribution of 14.7% and can be significantly separated from other modes according to the North criterion (North et al. 1982). As shown in Fig. 2a, large loadings of this mode are located to the south of the Yangtze River, with a consistent positive sign. Additionally, there are also negative loadings between the Yangtze and Yellow Rivers, but the values are relatively smaller. To highlight the interannual variations of the spring PIV over SC, we further perform the EOF analysis over the region of 21°–29°N, 110°–122°E. As shown in Fig. 2b, the first mode (EOF1) still displays a uniform pattern over SC with a variance contribution of 23.6% and can be significantly separated from other modes according to the North criterion. Such a result also indicates that the EOF1 mode over SC is not sensitive to the selection of domain for EOF analysis.

Figure 2c shows the normalized principal component of EOF1 (PC1). PC1 exhibits strong interannual variations during the past half-century. Additionally, it exhibits a significant correlation with the 7–25-day variability of SC-averaged spring precipitation on the interannual time scale, with a correlation coefficient of 0.8 (significant at the 99% confidence level). The region east of 110°E and south of 28°N with large loadings is chosen as the SC domain, and the following all refer to this region. There are 77 observation stations over the region. These results indicate that the intraseasonal variability of spring precipitation exhibits consistent interannual variations over SC, which could be well represented by PC1. In addition, we also analyze the interannual correlation between PC1 and spring total precipitation averaged over SC, and the correlation coefficient is 0.85, significant at the 99% confidence level, implying that the intraseasonal variability of precipitation

Brought to you by INSTITUTE OF ATMOSPHERIC PHYSICS, CAS | Unauthenticated | Downloaded 07/13/23 02:29 PM UTC

dominates the total precipitation variations over SC. Moreover, the intraseasonal variability of SC-averaged daily precipitation in spring could explain about 15.5% of the total daily precipitation variability during 1961–2019.

To understand the interannual variations in spring PIV over SC, we select intraseasonal precipitation events from the strong and weak PIV years. The anomalous PIV years are identified based on the normalized detrended PC1 (the insignificant increase trend is removed to better reflect interannual variation). The years with normalized detrend PC1 greater than 1 (less than −1) are regarded as the strong (weak) PIV years. Correspondingly, there are 11 strong years (1961, 1973, 1980, 1984, 1987, 1988, 1998, 2006, 2014, 2016, and 2019) and 10 weak years (1963, 1974, 1991, 1994, 1995, 2002, 2007, 2011, 2017, and 2018) selected. Next, the intraseasonal precipitation events are selected from these anomalous PIV years. The selection process is as follows: We first obtain the normalized time series of 7–25-day filtered SC-averaged daily precipitation in all springs and then select the peak days with normalized precipitation greater than one standard deviation. To highlight the features of spring, the peak days in the first week of March are excluded. Additionally, the time interval between two adjacent peak precipitation days must be 10 days or more; otherwise, the day with a larger normalized precipitation value is chosen. Then, 44 intraseasonal precipitation events are selected in the strong PIV years, and 30 intraseasonal precipitation events are selected in the weak PIV years.

To explore the reasons for the interannual variations in PIV, we perform a lead–lag composite of the 7–25-day filtered precipitation anomalies associated with the selected events from day −3 to day +2. Here, day 0 denotes the peak day of intraseasonal precipitation events, and the minus (plus) sign means the days lead (lag) the peak day. As illustrated in Figs. 3a–f, in strong PIV years, precipitation anomalies are weak in SC on day −3; afterward, positive precipitation anomalies gradually intensify in SC and reach a peak with maximum values greater than 8 mm day$^{-1}$ on day 0. Additionally, weak negative precipitation anomalies could be observed in a small area to the north of the Yangtze River. From day 0 onward, positive precipitation anomalies in SC gradually decrease; in contrast, weak negative anomalies gradually expand and extend southward.

In weak PIV years (Figs. 3g–l), intraseasonal precipitation anomalies over SC also show a "first increase and then decrease" feature from day −3 to day +2, with maximum values on day 0. However, compared with strong PIV years, the magnitude of positive precipitation anomalies in weak PIV years is much smaller, with values less than 6 mm day$^{-1}$ on day 0. Additionally, the boxplot of intraseasonal precipitation anomalies averaged in SC from day −1 to day +1 also suggests a larger intensity of intraseasonal precipitation events in strong PIV years (figure not shown). Therefore, we conclude that the interannual variations in spring PIV over SC could be mainly caused by the intensity of intraseasonal precipitation events.

In addition, we also carry out the same analyses using the CN05.1 precipitation data. The results show that there is a significant 7–25-day period in spring precipitation anomalies over southern China, and the first EOF mode of the standard deviation of 7–25-day filtered daily precipitation in spring exhibits a uniform pattern over southern China and can be significantly separated from other modes according to the North criterion (figure not shown). The correlation coefficient between the two PC1s derived from the station data and CN05.1 data is 0.93. Additionally, the intensity of intraseasonal precipitation events in strong PIV years is also larger than that in weak PIV years (figure not shown). Therefore, the results from the CN05.1 data could further verify our conclusions.

## 4. Causes of different intraseasonal precipitation intensity

In the last section, we suggest the interannual variations in spring PIV over SC are determined by the intensity of intraseasonal precipitation events, which raises another question: What is the reason for the difference in intraseasonal precipitation intensity between strong and weak PIV years? In this section, we strive to answer this question from the perspective of the local moisture budget, atmospheric circulations, and boundary forcings.

### *a. Local moisture budget*

According to the moisture continuity equation, precipitation anomalies are related to horizontal and vertical moisture advection (Chou et al. 2009), and moisture-budget diagnostics can quantify the relative contribution of the two advections to precipitation anomalies, which has been widely used in previous studies on intraseasonal precipitation (Xi et al. 2015; Hsu et al. 2016; Qi et al. 2019; Yao et al. 2020). Figure 4 gives the composited 7–25-day filtered moisture budget on the peak days of intraseasonal precipitation events in strong and weak PIV years and the corresponding differences. This result suggests that in both strong and weak PIV years, the vertical moisture transport shows the largest positive contribution, indicating its critical role in the intensity of intraseasonal precipitation (Figs. 4j,k). Additionally, local moisture change also has a positive contribution, but it is a small term compared with vertical moisture transport (Figs. 4a,b). In contrast, the horizontal moisture advection terms have little or even negative contributions to intraseasonal precipitation (Figs. 4d–i). Therefore, the intensity of intraseasonal precipitation mainly depends on vertical moisture transport. In comparison, the vertical moisture transport over SC in strong PIV years is much stronger than that in weak years, particularly over the south coast region with large EOF loadings (Fig. 4l). In addition, the meridional moisture transport is also larger in strong PIV years than that in weak years (Fig. 4i), whereas the other two terms are generally larger over SC in weak PIV years (Figs. 4c,f). Therefore, the vertical and meridional moisture transport could explain the larger intensity of intraseasonal precipitation events in strong PIV years.

Additionally, we further perform a time-scale separation of the vertical moisture transport term, referring to Hsu et al. (2011). Here, the low-frequency background state, intraseasonal variability, and synoptic-scale variability are represented by precipitation components with time scales greater than

Brought to you by INSTITUTE OF ATMOSPHERIC PHYSICS, CAS | Unauthenticated | Downloaded 07/13/23 02:29 PM UTC

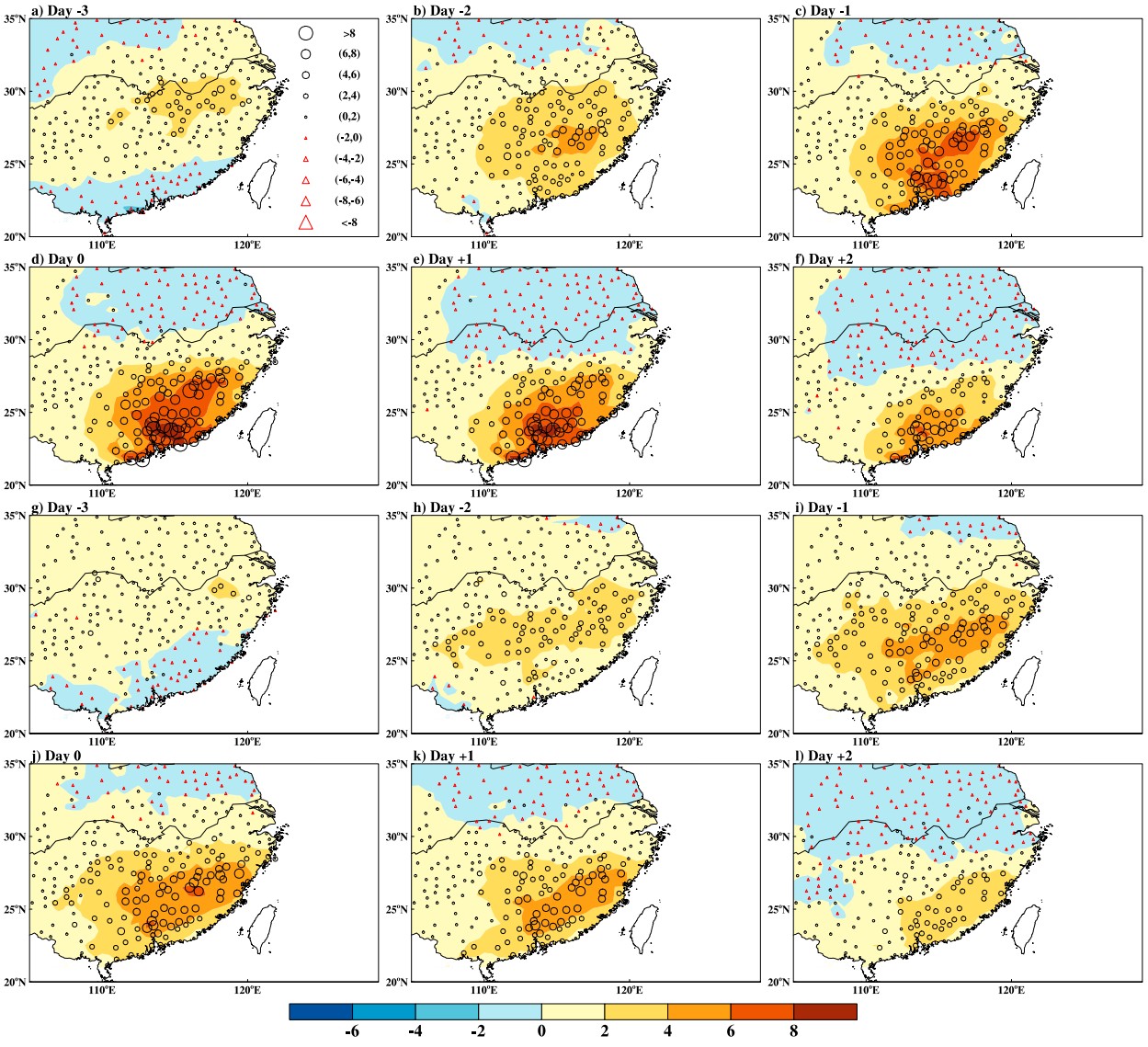


FIG. 3. (a)–(f) Lead–lag composited 7–25-day filtered precipitation anomalies (dotted and shaded; unit: mm day$^{-1}$) from day −3 to day +2 of intraseasonal precipitation events in strong PIV years. (g)–(l) As in (a)–(f), but for weak PIV years. Dots indicate precipitation anomalies at individual stations, and the shading is interpolated from the station precipitation based on the Cressman method.

25 days, between 7 and 25 days, and less than 7 days. Accordingly, the term $\langle \|\omega \partial q/\partial p\| \rangle'$ could be decomposed into nine subterms. The composited result from day −1 to day +1 indicates that the transport of low-frequency background moisture by intraseasonal vertical motion [i.e., $\langle \|\omega' \partial \overline{q}/\partial p\| \rangle'$] plays a decisive role in vertical moisture transport, and other terms are negligible (Fig. 5). In addition, the composited value of term $\langle \|\omega' \partial \overline{q}/\partial p\| \rangle'$ in strong PIV years is always larger than that in weak PIV years from day −1 to day +1, consistent with the aforementioned situations in vertical moisture transport and intraseasonal precipitation intensity over SC.

Figure 6 presents the composited 7–25-day filtered vertical motion averaged over 500–700 hPa from day −1 to day +1 of intraseasonal precipitation events in strong and weak PIV years. Consistent with the changes in precipitation anomalies in strong PIV years, significant upward motions dominate over SC from day −1 to day +1 (Figs. 6a–c). In weak years, significant upward motions could also be observed over SC but with lower intensity (Figs. 6d–f). Additionally, we also analyze the composited 850-hPa low-frequency background-specific humidity during intraseasonal precipitation events in strong and weak PIV years. The differences in specific humidity between strong and weak years are small over SC (figure not shown). Therefore, intraseasonal upward motion could be the main cause for the difference in intraseasonal precipitation intensity in strong and weak PIV years: stronger intraseasonal upward motion results in stronger intraseasonal precipitation intensity, and vice versa.

Brought to you by INSTITUTE OF ATMOSPHERIC PHYSICS, CAS | Unauthenticated | Downloaded 07/13/23 02:29 PM UTC

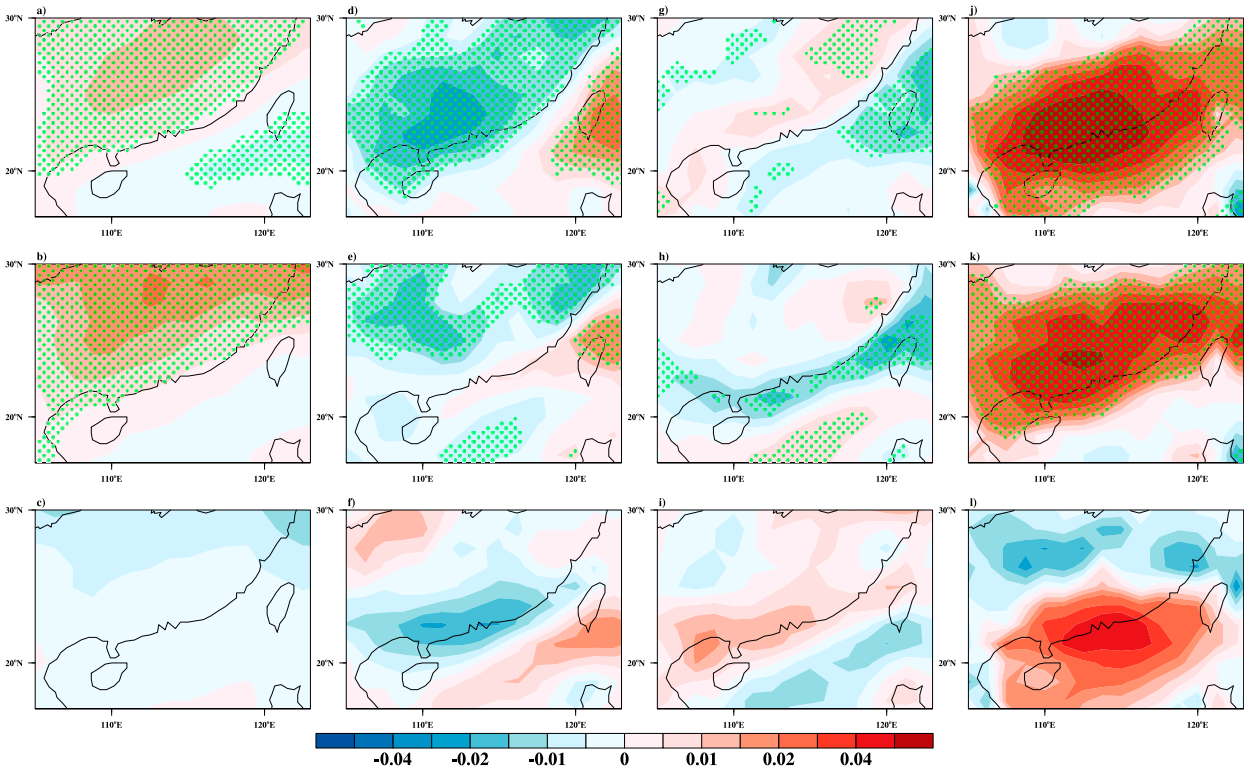


FIG. 4. Composited 7–25-day filtered local change in vertically integrated specific humidity from the surface to 300 hPa (shaded; unit: g $m^{-2}$ $s^{-1}$) on day 0 of intraseasonal precipitation events in (a) strong and (b) weak PIV years. (c) Differences between the composited results in (a) and (b). (d)–(f),(g)–(i),(j)–(l) As in (a)–(c), but for vertically integrated zonal moisture advection, meridional moisture advection, and vertical moisture advection, respectively. The dots represent the 90% confidence level.

### *b. Atmospheric circulations*

The analysis of the moisture budget in the last subsection suggests that vertical moisture transport caused by intraseasonal vertical motion plays a key role in the intraseasonal precipitation intensity. In this subsection, we further investigate the reasons for different intraseasonal vertical motion intensities in strong and weak PIV years.

We first diagnose the local mechanisms, using the quasigeostrophic omega equation (Holton 1992). Figure 7 gives the evolution of composited 7–25-day filtered precipitation anomalies and 500–700-hPa averaged dynamic and thermal terms of the omega equation averaged over SC in strong and weak PIV years, respectively. The evolution of the sum of dynamic and thermal terms is basically consistent with that of intraseasonal precipitation anomalies over SC, and both the dynamic and thermal terms show positive contributions. In comparison, corresponding to a larger intraseasonal precipitation intensity in stronger PIV years, the positive contribution of dynamic and thermal terms is also larger than that in weak years.

In more detail, the results of the time-scale separation of dynamic and thermal terms indicate that in strong PIV years, there are two major terms with positive contributions, that is, the zonal component of $\langle(\partial/\partial P)[\overline{\mathbf{V}}\cdot\boldsymbol{\nabla}(f+\zeta')]\rangle'$ and the meridional component of $\langle\nabla^2(\mathbf{V}'\cdot\boldsymbol{\nabla}\overline{T})\rangle'$, and the former occurs mainly on day −1 and day 0, while the latter could persist from day −1 to day +1 but gradually decrease (Figs. 8a–c). In addition, the zonal component of $\langle\nabla^2(\overline{\mathbf{V}}\cdot\boldsymbol{\nabla}T')\rangle'$ shows a positive contribution on day 0 and day +1, and the meridional component of $\langle(\partial/\partial P)[\mathbf{V}'\cdot\boldsymbol{\nabla}(f+\overline{\zeta})]\rangle'$ has a positive contribution on day +1 (Figs. 8b,c). In weak PIV years, as shown in Figs. 8d–f, there are four terms with relatively large positive contributions. The meridional component of $\langle(\partial/\partial P)[\overline{\mathbf{V}}\cdot\boldsymbol{\nabla}(f+\zeta')]\rangle'$ shows a positive contribution on day −1 and the meridional component of $\langle\nabla^2(\mathbf{V}'\cdot\boldsymbol{\nabla}\overline{T})\rangle'$ shows a positive contribution on day −1 and day 0. The former still shows positive contributions on day 0 and day +1 but is offset by the zonal component. Additionally, the zonal component of $\langle\nabla^2(\overline{\mathbf{V}}\cdot\boldsymbol{\nabla}T')\rangle'$ and the meridional component of $\langle(\partial/\partial P)[\mathbf{V}'\cdot\boldsymbol{\nabla}(f+\overline{\zeta})]\rangle'$ show positive contributions on day 0 and day +1. In comparison, the magnitudes of the main contributors in weak PIV years are smaller than those in strong PIV years. Briefly, although there are slight variations in the positive contribution term from day −1 to day +1, the main contributors to anomalous upward motions over SC in strong PIV years are zonal vorticity and meridional temperature advection, while those in weak PIV years are meridional vorticity and temperature advection.

To understand the physical process of the above-identified contributors taking effect, Fig. 9 first displays the associated local atmospheric circulation anomalies from day −1 to day +1 of intraseasonal precipitation events in strong PIV years. On day −1, an anomalous cyclone centers to the west of SC;

Brought to you by INSTITUTE OF ATMOSPHERIC PHYSICS, CAS | Unauthenticated | Downloaded 07/13/23 02:29 PM UTC

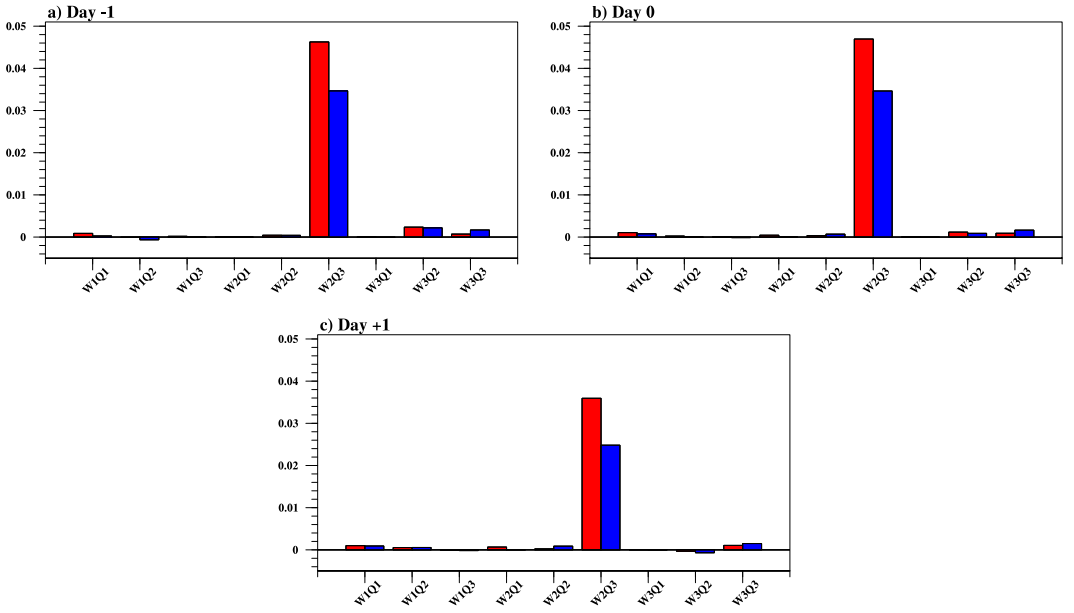


FIG. 5. Lead–lag composited 7–25-day filtered vertical integrated nine subterms of the term $\langle \omega \partial q/\partial p \rangle$ from surface to 300 hPa (shaded; unit: g m$^{-2}$ s$^{-1}$) averaged over SC from day −1 to day +1 of intraseasonal precipitation events in strong (red bars) and weak (blue bars) PIV years. Here, numbers 1, 2, and 3 on the horizontal axis denote synoptic-scale, intraseasonal, and low-frequency background state components, respectively, and the letters W and Q indicate vertical motion and specific humidity, respectively.

correspondingly, significant southerlies in the midtroposphere extend from the South China Sea to SC (Fig. 9a), which could lead to warm meridional temperature advection over SC due to warmer low-frequency background air temperature over the South China Sea, resulting in positive contributions of term $\nabla^2(v'\partial\overline{T}/\partial y)$. Additionally, such an anomalous cyclone is strongest in the upper troposphere, with a positive vorticity center there; concurrent with large low-frequency background westerlies, there are positive zonal vorticity advection anomalies $[-\overline{u}\partial\zeta'/\partial x > 0]$ in the mid–upper troposphere over SC (Fig. 9d). Because the low-frequency background zonal wind over SC in the lower troposphere is much weaker than that over the upper troposphere, the term $(\partial/\partial P)(\overline{u}\partial\zeta'/\partial x)$ could be positive over the region. In the following two days, the anomalous cyclone declines and propagates eastward toward SC; accordingly, anomalous midtroposphere southerlies over SC gradually weaken (Figs. 9b,c), resulting in decreased positive contributions of the term $\nabla^2(v'\partial\overline{T}/\partial y)$. Additionally, the positive vorticity center in the upper troposphere also declines and almost disappears on day +1 (Figs. 9e,f); therefore, the positive contributions of the term $(\partial/\partial P)(\overline{u}\partial\zeta'/\partial x)$ only persist to day 0.

However, corresponding to the eastward-moving cyclone, the associated low air temperature to its north also propagates eastward, which increases the temperature difference between SC and its upstream region. Concurrent with large low-frequency background southwesterlies over SC, the term $\nabla^2(\overline{u}\partial T'/\partial x)$ could make a positive contribution on day 0 and day +1 (Figs. 9g–i). Additionally, anomalous northerlies also strengthen in the mid–upper troposphere of SC on day +1 and, combined with the positive meridional low-frequency background vorticity gradient, the meridional vorticity advection is enhanced $[-v'\partial\overline{\zeta}/\partial y > 0]$ in the mid–upper troposphere over SC on day +1 (Figs. 9j–l), favoring the positive contributions of term $(\partial/\partial P)(v'\partial\overline{\zeta}/\partial y)$.

In weak PIV years, on day −1, anomalous cyclonic circulation in the midtroposphere is centered at the upper to middle reaches of the Yangtze River, and significant southwesterlies prevail over SC (Fig. 10a), also resulting in a large positive contribution of the term $\nabla^2(v'\partial\overline{T}/\partial y)$, whereas the magnitude is slightly smaller than that in strong PIV years because of the relatively weak southerlies, which could be demonstrated by the differences in composited intraseasonal horizontal winds between strong and weak PIV years (figure not shown). Additionally, as shown in Fig. 10d, corresponding to this cyclone, in the lower troposphere, significant positive vorticity anomalies occur in the north of SC, with negative vorticity anomalies to the south; therefore, there are positive meridional vorticity gradient anomalies in the lower troposphere over SC $(\partial\zeta'/\partial y > 0)$. In contrast, the meridional vorticity gradient in the mid–upper troposphere is relatively weak (400–500 hPa). Combined with low-frequency background southerlies over SC, the term $(\partial/\partial P)(\overline{v}\partial\zeta'/\partial y)$ shows positive contributions on day −1.

As the cyclone propagates eastward, anomalous southerlies over SC gradually weaken and turn into westerlies on day +1 (Figs. 10b,c), leading to decreased positive contributions of the term $\nabla^2(v'\partial\overline{T}/\partial y)$. However, the lower-troposphere positive vorticity anomalies north of SC are still significant (Figs. 10e,f); therefore, the positive contributions of the term $(\partial/\partial P)(\overline{v}\partial\zeta'/\partial y)$ could persist on day 0 and day +1. Moreover, along with the

Brought to you by INSTITUTE OF ATMOSPHERIC PHYSICS, CAS | Unauthenticated | Downloaded 07/13/23 02:29 PM UTC

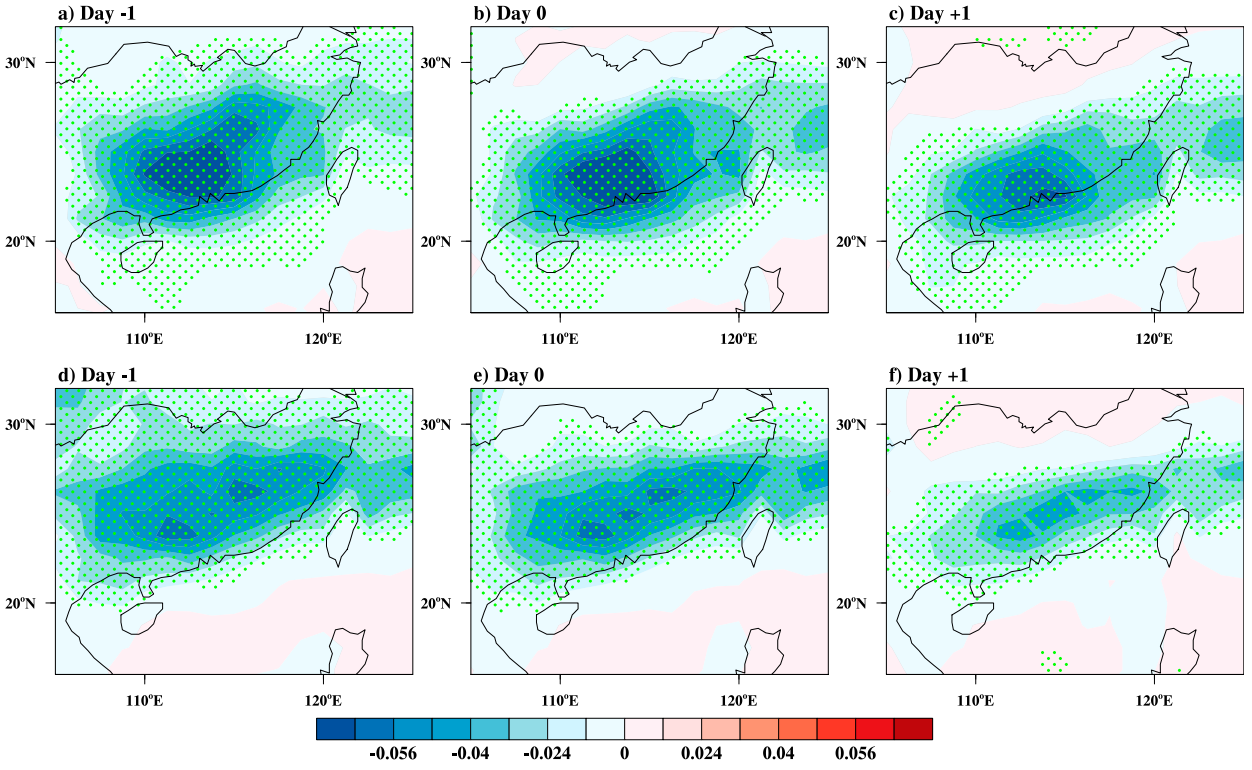


FIG. 6. (a)–(c) Lead–lag composited 7–25-day filtered vertical motion averaged over 500–700 hPa (shaded; unit: Pa $s^{-1}$) from day −1 to day +1 of intraseasonal precipitation events in strong PIV years. (d)–(f) As in (a)–(c), but for weak PIV years. The dots represent the 90% confidence level.

propagation of the cyclone, the related low air temperature also propagates eastward, concurring with large low-frequency background southwesterlies over SC (Figs. 10g–i). Additionally, anomalous northerlies also strengthen in the mid–upper troposphere of SC and combine with the positive meridional low-frequency background vorticity gradient (Figs. 10j,k). Therefore, the terms $\nabla^2(\overline{u}\partial T'/\partial x)$ and $(\partial/\partial P)(v'\partial\overline{\zeta}/\partial y)$ show a positive contribution on day 0 and day +1, which is similar to the situation in the strong PIV years.

The aforementioned analyses explore the local mechanisms for the upward motion over SC during intraseasonal precipitation events in strong and weak PIV years. Next, we strive to further investigate the associated large-scale atmospheric circulations responsible for such local mechanisms. Figure 11 shows the composited, 7–25-day, filtered geopotential height at 500 hPa from day −6 to day +1 of intraseasonal precipitation events in strong and weak PIV years. In strong years, on day −6, there are positive geopotential anomalies over the midlatitude North Atlantic centered around the west of Britain. Associated with this anomalous center and the wave activity flux, two wave trains propagate eastward from the North Atlantic to Asia along the northern and southern paths (Fig. 11a). The Eurasian southern and northern wave trains have been revealed to influence the winter climate over China

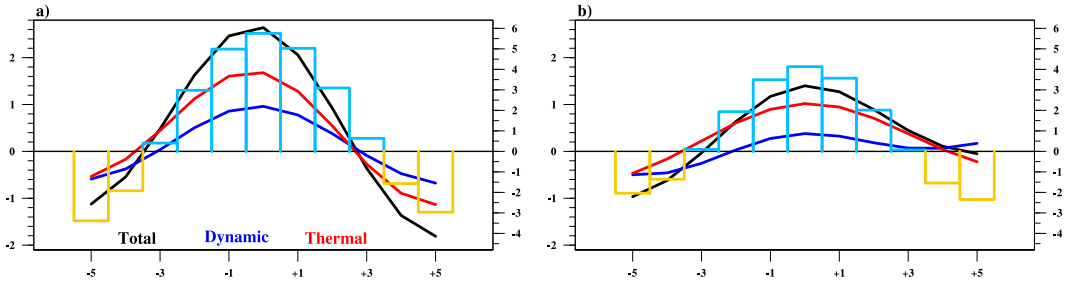


FIG. 7. Evolution of composited 7–25-day filtered precipitation anomalies (bars; unit: mm $day^{-1}$; right axis) and 500–700-hPa averaged dynamic (blue line; unit: $10^{-19}$ m $s^{-1}$ $kg^{-1}$; left axis) and thermal (red line; unit: $10^{-19}$ m $s^{-1}$ $kg^{-1}$; left axis) terms of the omega equation and their sum (black line; unit: $10^{-19}$ m $s^{-1}$ $kg^{-1}$; left axis) averaged over SC from day −5 to day +5 of intraseasonal precipitation events in (a) strong and (b) weak PIV years.

Brought to you by INSTITUTE OF ATMOSPHERIC PHYSICS, CAS | Unauthenticated | Downloaded 07/13/23 02:29 PM UTC

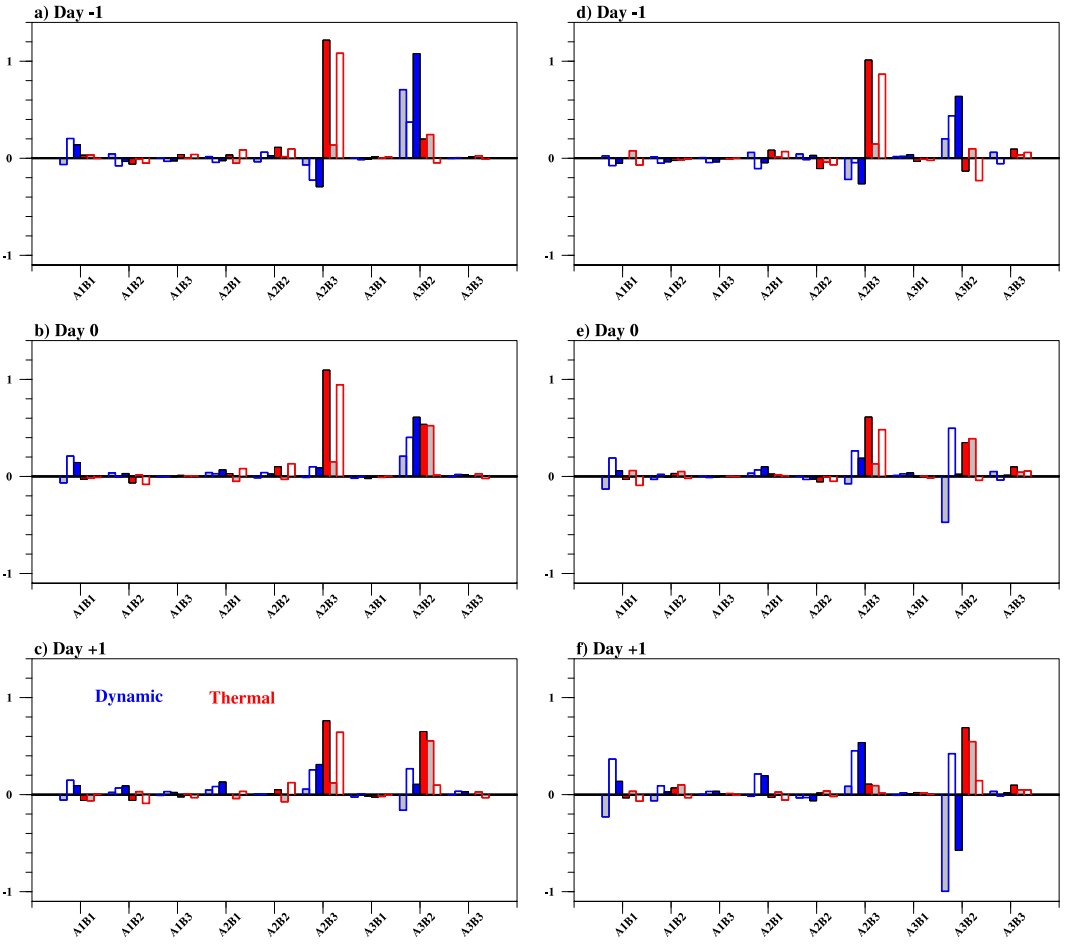


FIG. 8. (a)–(c) Lead–lag composited 7–25-day filtered nine subterms of the dynamic term (blue solid bars; unit: $10^{-19}$ m s$^{-1}$ kg$^{-1}$) and thermal term (red solid bars; unit: $10^{-19}$ m s$^{-1}$ kg$^{-1}$) averaged over 500–700 hPa over SC from day −1 to day +1 of intraseasonal precipitation events in strong PIV years. The gray and white bars with blue (red) borders denote the zonal and meridional components of nine subterms of the dynamic (thermal) term, respectively. (d)–(f) As in (a)–(c), but for weak PIV years. Here, numbers 1, 2, and 3 on the horizontal axis denote synoptic-scale, intraseasonal, and low-frequency background state components, respectively, and letters A and B indicate horizontal wind and absolute vorticity (air temperature) in the dynamic (thermal) term.

(Hu et al. 2018; Jiao et al. 2019; Li et al. 2020). This study indicates that they are also important for the spring intraseasonal precipitation over SC. On day −4, the structure of the two wave trains becomes more distinct (Fig. 11b). For the northern wave train, anomalous positive centers appear over the northeastern North Atlantic, northeastern Europe, and the East China Sea, and negative centers appear over the Scandinavian Peninsula and the Mongolian Plateau. For the southern wave train, the positive centers are over the northeastern North Atlantic, eastern Mediterranean, and northern Arabian Sea, and negative centers are over southwestern Europe, the south of the Caspian Sea, and the Bay of Bengal. Along with the eastward propagation of the two wave trains, the aforementioned two anomalous low pressures around the Bay of Bengal and Mongolian Plateau propagate eastward and merge, forming a low pressure extending from the Mongolian Plateau to the west of SC on day −2 (Fig. 11c). The low pressure continues to propagate eastward, and its southeastern part could reach SC in the next several days (Figs. 11d–f). Correspondingly, such anomalous low pressure leads to anomalous southerlies extending from the South China Sea to SC and an upper-troposphere positive vorticity centers to the west of SC, as shown in Figs. 9a–f. Additionally, the eastward propagation of low pressure also favors the invasion of cold air from Mongolia to SC, as shown in Figs. 9g–i, and intensified mid–upper troposphere northerlies in SC, as shown in Figs. 9j–l. Through the above physical processes, the southern and northern wave trains jointly contribute to upward motion and PIV over SC.

In weak years, there are also two similar wave trains over the region from the North Atlantic to Eurasia, although there are some visible differences in the location and intensity (Figs. 11g–l). Similarly, associated with the eastward propagation of the northern wave train, the anomalous low pressure around the Mongolian Plateau gradually propagates eastward

Brought to you by INSTITUTE OF ATMOSPHERIC PHYSICS, CAS | Unauthenticated | Downloaded 07/13/23 02:29 PM UTC

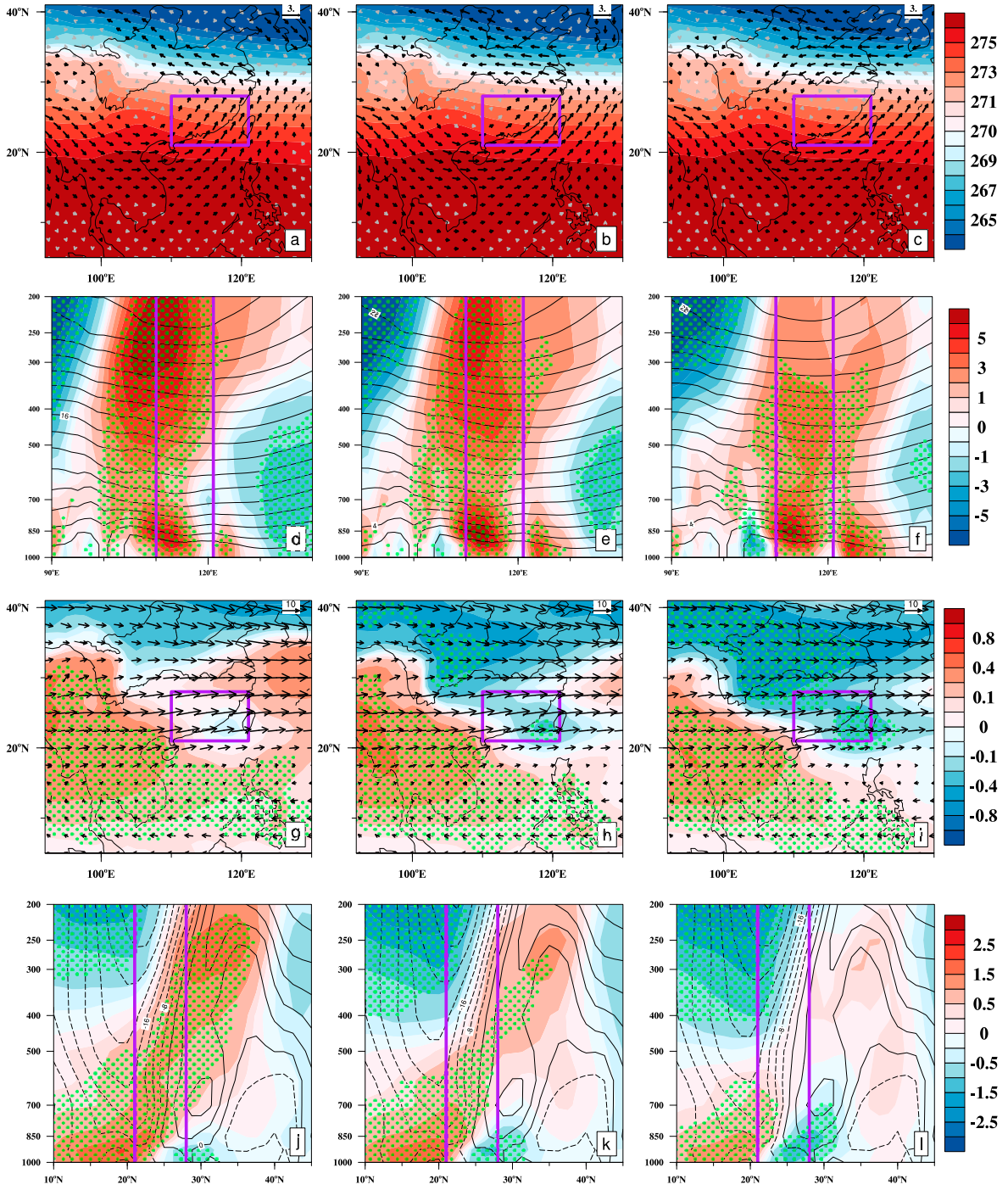


FIG. 9. (a)–(c) Lead–lag composited 7–25-day filtered horizontal winds (arrows; unit: m $s^{-1}$) and low-frequency background air temperature (shaded; unit: K) averaged over 500–700 hPa from day −1 to day +1 of intraseasonal precipitation events in strong PIV years. (d)–(f) Longitude–pressure cross sections of lead–lag composited 7–25-day filtered relative vorticity (shaded; unit: $10^{-6}$ $s^{-1}$) and the low-frequency background zonal wind [solid (dashed) line for positive (negative) value; units: m $s^{-1}$] averaged over 21°–28°N from day −1 to day +1 of intraseasonal precipitation events in strong PIV years. (g)–(i) As in (a)–(c), but for low-frequency background horizontal winds (arrows; unit: m $s^{-1}$) and 7–25-day filtered air temperature (shaded; unit: K). (j)–(l) Latitude–pressure cross sections of lead–lag composited 7–25-day filtered meridional wind (shaded; units: m $s^{-1}$) and the low-frequency background relative vorticity [solid (dashed) line for positive (negative) value; unit: $10^{-6}$ $s^{-1}$] averaged over 110°–121°E from day −1 to day +1 of intraseasonal precipitation events in strong PIV years. The black arrows in (a)–(c) and dots in (d)–(l) represent the 90% confidence level. The boxes in (a)–(c) and (g)–(i) indicate the key region of SC, and the thick lines in (d)–(f) and (j)–(l) indicate the longitudinal and latitudinal range of SC.

Brought to you by INSTITUTE OF ATMOSPHERIC PHYSICS, CAS | Unauthenticated | Downloaded 07/13/23 02:29 PM UTC

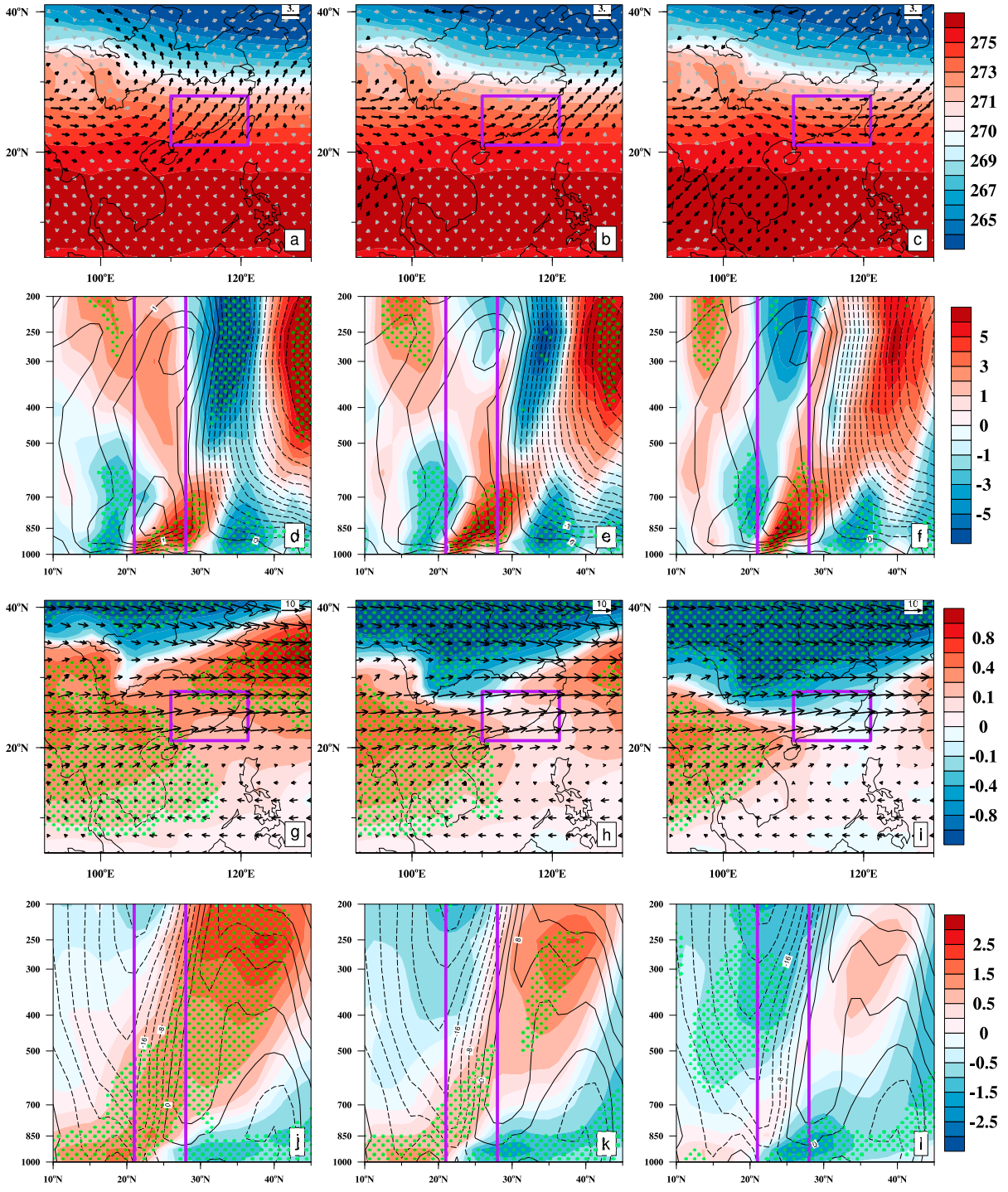


FIG. 10. (a)–(c) Lead–lag composited 7–25-day filtered horizontal winds (arrows; unit: m $s^{-1}$) and low-frequency background air temperature (shaded; unit: K) averaged over 500–700 hPa from day −1 to day +1 of intraseasonal precipitation events in weak PIV years. (d)–(f) Latitude–pressure cross section of lead–lag composited 7–25-day filtered relative vorticity (shaded; unit: $10^{-6}$ $s^{-1}$) and the low-frequency background meridional wind [solid (dashed) line for positive (negative) value; units: m $s^{-1}$] averaged over 110°–121°E from day −1 to day +1 of intraseasonal precipitation events in weak PIV years. (g)–(i) As in (a)–(c), but for low-frequency background horizontal winds (arrows; unit: m $s^{-1}$) and 7–25-day filtered air temperature (shaded; unit: K). (j)–(l) As in (d)–(f), but for 7–25-day filtered meridional wind (shaded; units: m $s^{-1}$) and the low-frequency background relative vorticity [solid (dashed) line for positive (negative) value; unit: $10^{-6}$ $s^{-1}$]. The black arrows in (a)–(c) and dots in (d)–(l) represent the 90% confidence level. The boxes in (a)–(c) and (g)–(i) indicate the key region of SC, and the thick lines in (d)–(f) and (j)–(l) indicate the latitudinal range of SC.

Brought to you by INSTITUTE OF ATMOSPHERIC PHYSICS, CAS | Unauthenticated | Downloaded 07/13/23 02:29 PM UTC

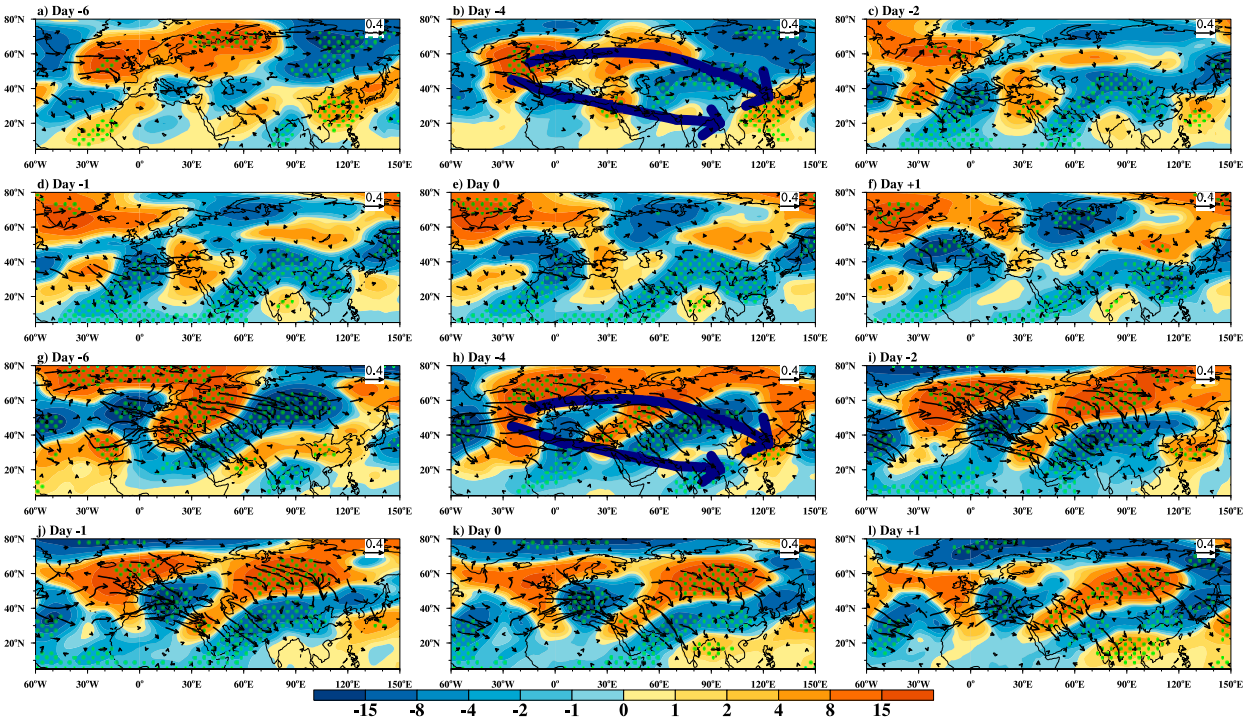


FIG. 11. Composited 7–25-day filtered geopotential height (shaded; unit: gpm) at 500 hPa and the corresponding horizontal wave activity flux (black arrows; units: $m^2\ s^{-2}$) at (a) day −6, (b) day −4, (c) day −2, (d) day –1, (e) day 0, and (f) day +1 of intraseasonal precipitation events in strong PIV years. (g)–(l) As in (a)–(f), but for weak PIV years. The dots represent the 90% confidence level. The thick blue arrows shown in (b) and (h) indicate the propagation path of two wave trains.

and could reach the upper–middle reaches of the Yangtze River on day −1 and day 0, and the downstream high pressure propagates to the south of Japan (Figs. 11j,k). In contrast, although the anomalous low pressure of the southern wave train is around the Bay of Bengal on day −4, it does not propagate eastward further to SC as in strong PIV years. Instead, it decays and is gradually replaced by the high pressure from day −2 (Figs. 11h–l). The difference in the propagation of the anomalous low pressure around the Bay of Bengal between strong and weak PIV years could be demonstrated by the time–longitude cross section of composited intraseasonal geopotential heights at 500 hPa along 20°N. As shown in Fig. 12a, in strong PIV years, the anomalous low pressure around the Bay of Bengal gradually propagates eastward to SC. In contrast, the anomalous low pressure could not propagate to SC and is replaced by a high pressure in weak PIV years (Fig. 12b). Such a result further confirms that the anomalous low pressure around the Bay of Bengal in the southern wave train tends to further propagate eastward to SC in strong PIV years. Therefore, in weak PIV years, the northern wave train could play a major role in intraseasonal precipitation events over SC. The low pressure could cause anomalous southwesterlies over SC, as shown in Figs. 10a–c, and the lower-troposphere positive vorticity north of SC, as shown in Figs. 10d–f. Additionally, this low-pressure center could also be responsible for the variations in low air temperature and mid–upper troposphere northerlies shown in Figs. 10g–l. Through these physical processes, the northern wave train could lead to anomalous upward motion over SC, consequently contributing to the PIV over the region.

### c. *Boundary forcings*

The previous subsection suggests that the key difference between the atmospheric circulation anomalies associated with intraseasonal precipitation events in strong and weak PIV years is whether the southern wave train can propagate eastward further to SC and merge with the northern wave train. What causes such a difference in the propagation of the southern wave train? We attempt to answer this question from the perspective of boundary forcings.

Figures 13a and 13b show the regressed SST anomalies against the normalized detrended PC1 in spring and the preceding February. In strong PIV years, there are significant warm SST anomalies over the tropical Indian Ocean and the South China Sea, and the SST anomalies persist well from late winter to the following spring. Additionally, we also analyze the composite SST anomalies between strong and weak PIV years, and the findings are consistent with the regressed results (Figs. 13c,d). Associated with the large-scale SST warming over the above regions, significant land warming also occurs over the Indochina Peninsula, and the warming magnitude is larger than that of the ocean (Fig. 13e) because of the relatively small specific heat capacity of the land. Such SST and land warming could heat the overlying atmosphere; therefore, widespread significant atmospheric warming occurs over the low latitudes south of 20°N with a center in Indochina

Brought to you by INSTITUTE OF ATMOSPHERIC PHYSICS, CAS | Unauthenticated | Downloaded 07/13/23 02:29 PM UTC

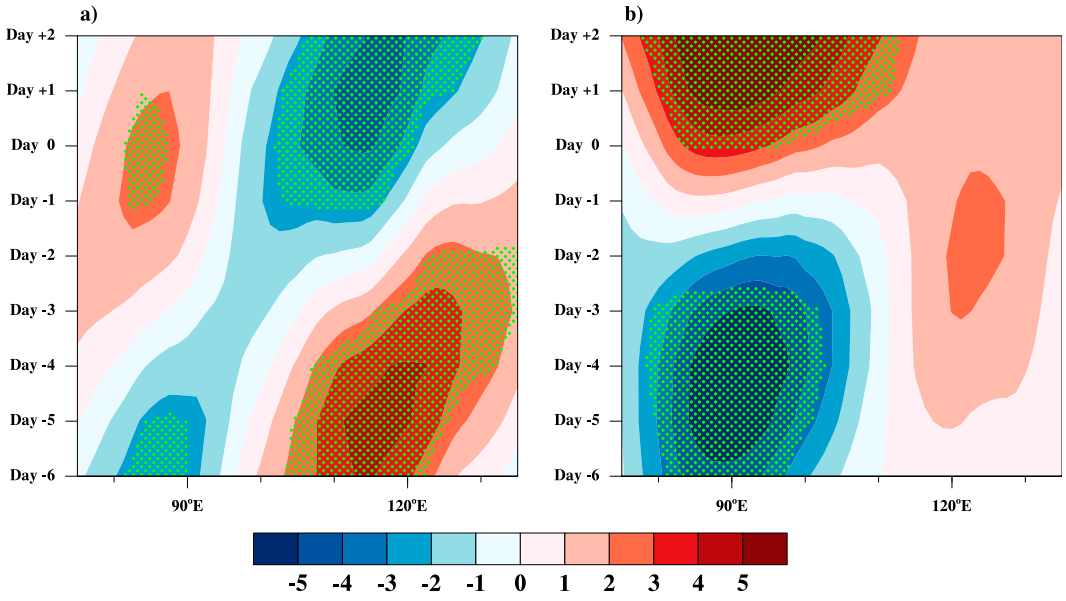


FIG. 12. Time–longitude cross sections of composited 7–25-day filtered geopotential heights (shaded; unit: gpm) at 500 hPa along 20°N from day −6 to day +2 of intraseasonal precipitation events in (a) strong and (b) weak PIV years. The dots represent the 90% confidence level.

Peninsula (Fig. 13f). According to the thermal wind principle, such atmospheric warming would result in intensified westerlies on its north side by increasing the atmospheric baroclinicity. Correspondingly, significant westerlies extend zonally from the north of the Bay of Bengal to the south of Japan (Fig. 13g). Additionally, we also compare the low-frequency background westerlies associated with intraseasonal precipitation events in strong and weak PIV years, and the enhanced westerlies north of the Bay of Bengal could also be observed in strong years (figure not shown). Due to the waveguiding effect of enhanced background westerlies (Watanabe 2004), the southern wave train could further propagate eastward to SC, therefore contributing to the stronger upward motion and PIV over SC.

To further investigate the relationship between the SST anomalies in the tropical Indian Ocean and the South China Sea and the PIV over SC, we further derive the time series of SST anomalies averaged over the key region (15°S–20°N, 85°–122°E; box in Figs. 13a–d). As shown in Fig. 13h, the PC1 covaries well with the spring SST index. The correlation coefficient between the two is 0.47, significant at the 99% confidence level. In addition, consistent with the results in Figs. 13b and 13d, the PC1 is also significantly correlated to the February SST index, with a coefficient of 0.36, significant at the 99% confidence level. Such a result indicates the possible role of the SST anomalies over the tropical Indian Ocean and the South China Sea in the interannual variations in spring PIV over SC.

## 5. Summary and discussion

In this study, the interannual variations in spring PIV over SC and related mechanisms are analyzed. The results show that spring precipitation over SC exhibits distinct intraseasonal variations with a significant period of 7–25 days, and the first mode of PIV displays a monopole pattern over SC on the interannual time scale. By comparing the intraseasonal precipitation events in strong and weak PIV years, it is suggested that the intensity of intraseasonal precipitation events determines the PIV magnitude, in which the intensity of intraseasonal upward motion plays a decisive role.

Associated atmospheric circulations are further investigated. In general, two atmospheric wave trains could be observed during intraseasonal precipitation events in both strong and weak PIV years. The wave trains propagate eastward from the North Atlantic to Asia across the low and mid–high latitudes of Eurasia and are named the southern and northern wave trains. In strong PIV years, intraseasonal precipitation events are jointly influenced by these two wave trains, as they can both propagate to East Asia. The two wave trains jointly lead to anomalous low pressure to the west of SC, which favors strong upward motion and PIV over SC by causing strong zonal vorticity and meridional temperature advection.

In weak PIV years, the northern wave train can propagate to East Asia, whereas the southern wave train cannot. The southern wave train can only propagate to the Bay of Bengal. Accordingly, the northern wave train leads to an anomalous low pressure over the upper–middle reaches of the Yangtze River, which further results in a weak upward motion and PIV over SC by causing weak meridional vorticity and temperature advection.

To understand the reasons for the eastward propagation of the southern wave train, the boundary conditions are further analyzed. It is found that in strong PIV years, there are significant warming SST anomalies over the tropical Indian Ocean and the South China Sea. The warming SST could heat the overlying atmosphere and further enhance the meridional temperature gradient between the tropical region and midlatitude Asia.

Brought to you by INSTITUTE OF ATMOSPHERIC PHYSICS, CAS | Unauthenticated | Downloaded 07/13/23 02:29 PM UTC

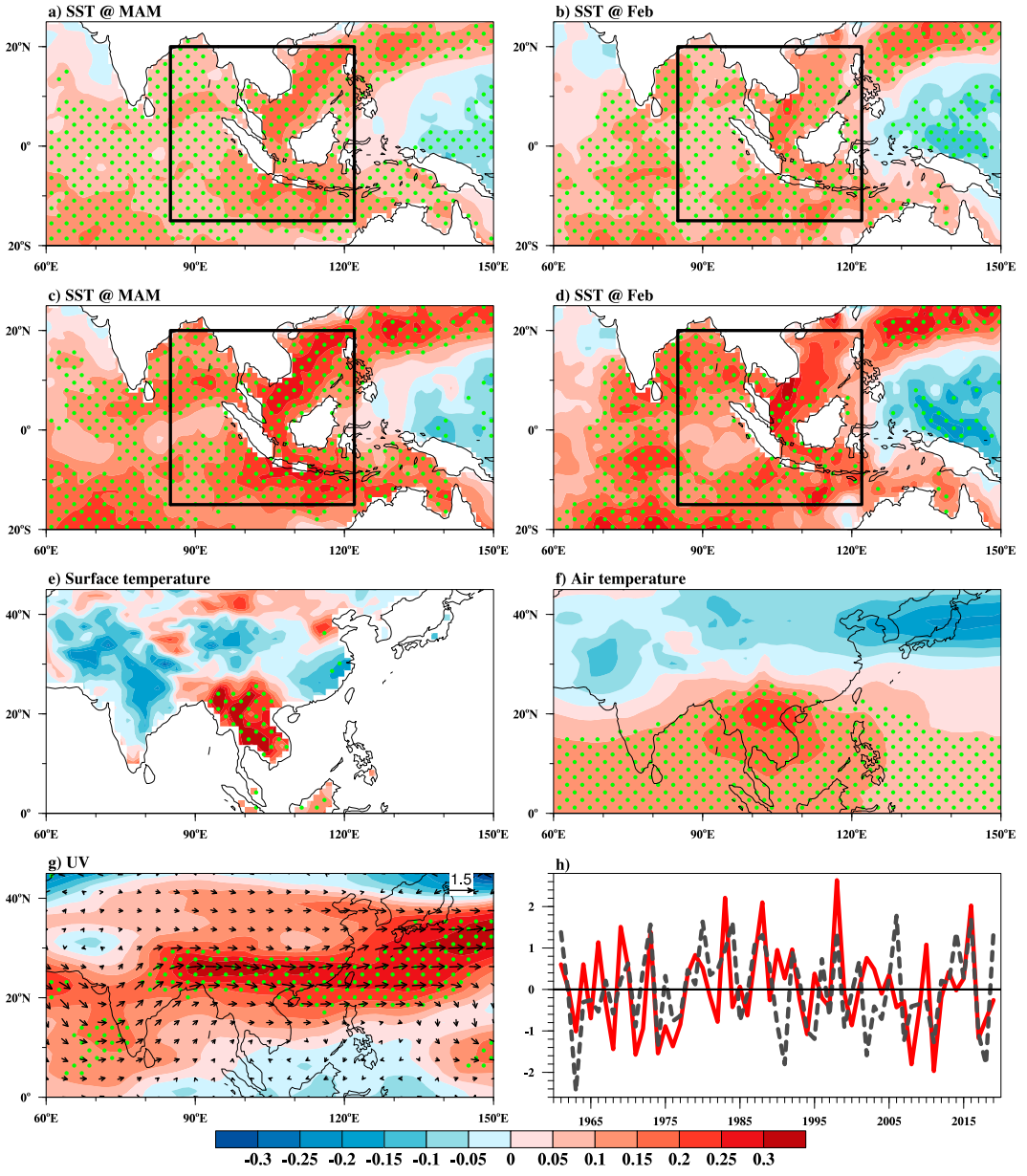


FIG. 13. Linear regressions of (a) spring SST (shaded; unit: K), (b) February SST (shaded; unit: K), (e) surface temperature in spring (shaded; unit: K), (f) air temperature averaged over 500–850 hPa in spring (shaded; unit: K), and (g) zonal wind (shaded; unit: 3 m $s^{-1}$) and horizontal wind (arrows; unit: m $s^{-1}$) at 300 hPa in spring, against the normalized detrended PC1 during 1961–2019. (c),(d) Composite differences in SST anomalies (shaded; unit: 2 K) in spring and February between the strong and weak PIV years. The dots represent the 90% confidence level. (h) The normalized time series of the detrended PC1 (dashed line) and spring SST index (solid line).

According to the thermal wind principle, the background westerlies are significantly enhanced and extend from the north of the Bay of Bengal to the south of Japan. Owing to the waveguiding effect of enhanced background westerlies, the southern wave train could propagate further eastward from the Bay of Bengal to SC and consequently contribute to strong upward motion and PIV over SC. In addition, the significant interannual correlation between the SST index of the tropical Indian Ocean to South China Sea and PC1 also implies the important roles of the aforementioned SST conditions in the interannual variations in spring PIV over SC.

This study investigates the interannual variations in spring PIV over SC and suggests a close relationship between the PIV magnitude and the intensity of intraseasonal precipitation events over the region. It has been reported that intraseasonal oscillation could have important contributions to the occurrence of heavy precipitation events over SC (Miao et al. 2019; Zheng et al. 2022; Liu et al. 2023), and the analyses in

Brought to you by INSTITUTE OF ATMOSPHERIC PHYSICS, CAS | Unauthenticated | Downloaded 07/13/23 02:29 PM UTC

this study further indicate that the interannual background of intraseasonal oscillation should also be considered when analyzing heavy precipitation events over SC: the years with a larger PIV magnitude generally imply a higher probability of occurrence of heavy precipitation events. More importantly, the PIV magnitude over SC is significantly correlated with the SST anomalies over the tropical Indian Ocean and the South China Sea in the preceding February. So these preceding SST anomalies could provide valuable information for the prediction of the PIV magnitude over SC, which could further benefit the prediction of heavy rainfall events over SC.

*Acknowledgments.* This study was supported by the National Natural Science Foundation of China (Grant 41825010).

*Data availability statement.* Daily station precipitation data in China can be accessed from http://data.cma.cn/. The Japanese 55-year Reanalysis dataset can be downloaded from https://rda.ucar.edu/datasets/ds628.0/. The Hadley SST dataset is derived from https://www.metoffice.gov.uk/hadobs/hadisst/.

## REFERENCES

Cheng, Y., L. Wang, and T. Li, 2020: Causes of interdecadal increase in the intraseasonal rainfall variability over southern China around the early 1990s. *J. Climate*, **33**, 9481–9496, https://doi.org/10.1175/JCLI-D-20-0047.1.

Cheng, Z., Y. Qiao, M. Jian, and S. T. Siems, 2018: Inter-decadal change of leading pattern of spring rainfall over southern China during 1901–2010. *Int. J. Climatol.*, **38**, 3494–3512, https://doi.org/10.1002/joc.5511.

Chou, C., J. D. Neelin, C.-A. Chen, and J.-Y. Tu, 2009: Evaluating the "rich-get-richer" mechanism in tropical precipitation change under global warming. *J. Climate*, **22**, 1982–2005, https://doi.org/10.1175/2008JCLI2471.1.

Cressman, G. P., 1959: An operational objective analysis system. *Mon. Wea. Rev.*, **87**, 367–374, https://doi.org/10.1175/1520-0493(1959)087<0367:AOOAS>2.0.CO;2.

Deng, L., and T. Li, 2016: Relative roles of background moisture and vertical shear in regulating interannual variability of boreal summer intraseasonal oscillations. *J. Climate*, **29**, 7009–7025, https://doi.org/10.1175/JCLI-D-15-0498.1.

Duchon, C. E., 1979: Lanczos filtering in one and two dimensions. *J. Appl. Meteor.*, **18**, 1016–1022, https://doi.org/10.1175/1520-0450(1979)018<1016:LFIOAT>2.0.CO;2.

Feng, J., and J. Li, 2011: Influence of El Niño Modoki on spring rainfall over south China. *J. Geophys. Res.*, **116**, D13102, https://doi.org/10.1029/2010JD015160.

——, L. Yu, and D. Hu, 2014: Influence of Indian Ocean subtropical dipole on spring rainfall over China. *Int. J. Climatol.*, **34**, 954–963, https://doi.org/10.1002/joc.3732.

Gu, L., J. Sun, S. Yu, and M. Zhang, 2021: Footprints of Pacific decadal oscillation in the interdecadal variation of consecutive cloudy-rainy events in southern China. *Atmos. Res.*, **257**, 105609, https://doi.org/10.1016/j.atmosres.2021.105609.

Gu, W., L. Wang, Z.-Z. Hu, K. Hu, and Y. Li, 2018: Interannual variations of the first rainy season precipitation over South China. *J. Climate*, **31**, 623–640, https://doi.org/10.1175/JCLI-D-17-0284.1.

Han, J., and R. Zhang, 2022: Influence of preceding North Atlantic Oscillation on the spring precipitation in the middle and lower reaches of the Yangtze River valley. *Int. J. Climatol.*, **42**, 4728–4739, https://doi.org/10.1002/joc.7500.

Holton, J. R., 1992: *An Introduction to Dynamic Meteorology*. 3rd ed. Academic Press, 511 pp.

Hsu, P.-C., T. Li, and C.-H. Tsou, 2011: Interactions between boreal summer intraseasonal oscillations and synoptic-scale disturbances over the western North Pacific. Part I: Energetics diagnosis. *J. Climate*, **24**, 927–941, https://doi.org/10.1175/2010JCLI3833.1.

——, J.-Y. Lee, and K.-J. Ha, 2016: Influence of boreal summer intraseasonal oscillation on rainfall extremes in southern China. *Int. J. Climatol.*, **36**, 1403–1412, https://doi.org/10.1002/joc.4433.

Hu, K., G. Huang, R. Wu, and L. Wang, 2018: Structure and dynamics of a wave train along the wintertime Asian jet and its impact on East Asian climate. *Climate Dyn.*, **51**, 4123–4137, https://doi.org/10.1007/s00382-017-3674-1.

Huang, D.-Q., J. Zhu, Y.-C. Zhang, J. Wang, and X.-Y. Kuang, 2015: The impact of the East Asian subtropical jet and polar front jet on the frequency of spring persistent rainfall over southern China in 1997–2011. *J. Climate*, **28**, 6054–6066, https://doi.org/10.1175/JCLI-D-14-00641.1.

Jia, X., D. R. Cao, J. W. Ge, and M. Wang, 2018: Interdecadal change of the impact of Eurasian snow on spring precipitation over southern China. *J. Geophys. Res. Atmos.*, **123**, 10 092–10 108, https://doi.org/10.1029/2018JD028612.

Jiang, P., and P. Zhao, 2012: The interannual variability of spring rainy belt over southern China and the associated atmospheric circulation anomalies (in Chinese). *Acta Meteor. Sin.*, **70**, 681–689, https://doi.org/10.11676/qxxb2012.055.

Jiang, Z., D.-L. Zhang, and H. Liu, 2020: Roles of synoptic to quasi-monthly disturbances in generating two pre-summer heavy rainfall episodes over South China. *Adv. Atmos. Sci.*, **37**, 211–228, https://doi.org/10.1007/s00376-019-8156-4.

Jiao, Y., R. Wu, and L. Song, 2019: Individual and combined impacts of two Eurasian wave trains on intraseasonal East Asian winter monsoon variability. *J. Geophys. Res. Atmos.*, **124**, 4530–4548, https://doi.org/10.1029/2018JD029953.

Kobayashi, S., and Coauthors, 2015: The JRA-55 Reanalysis: General specifications and basic characteristics. *J. Meteor. Soc. Japan*, **93**, 5–48, https://doi.org/10.2151/jmsj.2015-001.

Li, C., T. Li, A. Lin, D. Gu, and B. Zheng, 2015: Relationship between summer rainfall anomalies and sub-seasonal oscillations in South China. *Climate Dyn.*, **44**, 423–439, https://doi.org/10.1007/s00382-014-2172-y.

Li, L., G. Xu, and Y. Liu, 2014: Influences of low-frequency moisture transportation on low frequency precipitation anomalies in the annually first rain season of South China in 2010 (in Chinese). *J. Trop. Meteor.*, **30**, 423–431.

Li, W., P.-C. Hsu, J. He, Z. Zhu, and W. Zhang, 2016: Extended-range forecast of spring rainfall in southern China based on the Madden–Julian Oscillation. *Meteor. Atmos. Phys.*, **128**, 331–345, https://doi.org/10.1007/s00703-015-0418-9.

Li, X., Z. Wen, and W.-R. Huang, 2020: Modulation of South Asian jet wave train on the extreme winter precipitation over Southeast China: Comparison between 2015/16 and 2018/19. *J. Climate*, **33**, 4065–4081, https://doi.org/10.1175/JCLI-D-19-0678.1.

Li, Z., S. Yang, B. He, and C. Hu, 2016: Intensified springtime deep convection over the South China Sea and the Philippine

Brought to you by INSTITUTE OF ATMOSPHERIC PHYSICS, CAS | Unauthenticated | Downloaded 07/13/23 02:29 PM UTC

Sea dries southern China. *Sci. Rep.*, **6**, 30470, https://doi.org/10.1038/srep30470.

Lin, A., Z. Ji, D. Gu, C. Li, B. Zheng, and C. He, 2016: Application of atmospheric intraseasonal oscillation in precipitation forecast over South China (in Chinese). *J. Trop. Meteor.*, **32**, 878–889.

——, D. Gu, C. Li, B. Zheng, and D. Peng, 2022: Atmospheric circulation and sea surface temperature anomalies associated with the interannual variation of persistent heavy precipitation in flood season of South China (in Chinese). *J. Trop. Meteor.*, **38**, 1–10.

LinHo, L. H., X. Huang, and N.-C. Lau, 2008: Winter-to-spring transition in East Asia: A planetary-scale perspective of the South China spring rain onset. *J. Climate*, **21**, 3081–3096, https://doi.org/10.1175/2007JCLI1611.1.

Liu, H., R. Yan, B. Wang, G. Chen, J. Ling, and S. Fu, 2023: Multiscale combined action and disturbance characteristics of pre-summer extreme precipitation events over South China. *Adv. Atmos. Sci.*, **40**, 824–842, https://doi.org/10.1007/s00376-021-1172-1.

Lu, R., Z. Zhu, T. Li, and H. Zhang, 2020: Interannual and interdecadal variabilities of spring rainfall over northeast China and their associated sea surface temperature anomaly forcings. *J. Climate*, **33**, 1423–1435, https://doi.org/10.1175/JCLI-D-19-0302.1.

Lu, T., Z. Zhu, Y. Yang, J. Ma, and G. Huang, 2023: Formation mechanism of the ENSO-independent summer western North Pacific anomalous anticyclone. *J. Climate*, **36**, 1711–1726, https://doi.org/10.1175/JCLI-D-22-0271.1.

Miao, R., M. Wen, R. Zhang, and L. Li, 2019: The influence of wave trains in mid-high latitudes on persistent heavy rain during the first rainy season over South China. *Climate Dyn.*, **53**, 2949–2968, https://doi.org/10.1007/s00382-019-04670-y.

Nie, Y., and J. Sun, 2022: Causes of interannual variability of summer precipitation intraseasonal oscillation intensity over southwest China. *J. Climate*, **35**, 3705–3723, https://doi.org/10.1175/JCLI-D-21-0627.1.

North, G. R., T. L. Bell, R. F. Cahalan, and F. J. Moeng, 1982: Sampling errors in the estimation of empirical orthogonal functions. *Mon. Wea. Rev.*, **110**, 699–706, https://doi.org/10.1175/1520-0493(1982)110<0699:SEITEO>2.0.CO;2.

Pan, W., J. Mao, and G. Wu, 2013: Characteristics and mechanism of the 10–20-day oscillation of spring rainfall over southern China. *J. Climate*, **26**, 5072–5087, https://doi.org/10.1175/JCLI-D-12-00618.1.

Park, C.-K., D.-S. R. Park, C.-H. Ho, T.-W. Park, J. Kim, S. Jeong, and B.-M. Kim, 2020: A dipole mode of spring precipitation between southern China and Southeast Asia associated with the eastern and central Pacific types of ENSO. *J. Climate*, **33**, 10 097–10 111, https://doi.org/10.1175/JCLI-D-19-0625.1.

Qi, Y., T. Li, R. Zhang, and Y. Chen, 2019: Interannual relationship between intensity of rainfall intraseasonal oscillation and summer-mean rainfall over Yangtze River Basin in eastern China. *Climate Dyn.*, **53**, 3089–3108, https://doi.org/10.1007/s00382-019-04680-w.

Qiang, X.-M., and X.-Q. Yang, 2013: Relationship between the first rainy season precipitation anomaly in South China and the sea surface temperature anomaly in the Pacific (in Chinese). *Chin. J. Geophys.*, **56**, 2583–2593, https://doi.org/10.6038/cjg20130808.

Qu, J., D. Gong, R. Mao, J. Yang, and S. Li, 2017: Possible influence of Arctic oscillation on precipitation along the East Asian rain belt during boreal spring. *Theor. Appl. Climatol.*, **130**, 487–495, https://doi.org/10.1007/s00704-016-1900-0.

Rayner, N. A., D. E. Parker, E. B. Horton, C. K. Folland, L. V. Alexander, D. P. Rowell, E. C. Kent, and A. Kaplan, 2003: Global analyses of sea surface temperature, sea ice, and night marine air temperature since the late nineteenth century. *J. Geophys. Res.*, **108**, 4407, https://doi.org/10.1029/2002JD002670.

Ren, Q., Z. Zhu, L. Hao, and J. He, 2017: The enhanced relationship between Southern China winter rainfall and warm pool ocean heat content. *Int. J. Climatol.*, **37**, 409–419, https://doi.org/10.1002/joc.4714.

Ren, Z., and Coauthors, 2015: Development of three-step quality control system of real-time observation data from AWS in China (in Chinese). *Meteor. Mon.*, **41**, 1268–1277.

Seager, R., and N. Henderson, 2013: Diagnostic computation of moisture budgets in the ERA-Interim reanalysis with reference to analysis of CMIP-archived atmospheric model data. *J. Climate*, **26**, 7876–7901, https://doi.org/10.1175/JCLI-D-13-00018.1.

Sun, J., and J. Ao, 2013: Changes in precipitation and extreme precipitation in a warming environment in China. *Chin. Sci. Bull.*, **58**, 1395–1401, https://doi.org/10.1007/s11434-012-5542-z.

Takaya, K., and H. Nakamura, 2001: A formulation of a phase-independent wave-activity flux for stationary and migratory quasigeostrophic eddies on a zonally varying basic flow. *J. Atmos. Sci.*, **58**, 608–627, https://doi.org/10.1175/1520-0469(2001)058<0608:AFOAPI>2.0.CO;2.

Tan, G., and Y. Wang, 2016: Combined effects of mid-to high-latitudes and the tropic on the low-frequency precipitation in Jiangnan from April to June (in Chinese). *Acta Meteor. Sin.*, **74**, 335–351, https://doi.org/10.11676/qxxb2016.032.

Wang, X.-F., Y. Chang, and Z.-Z. Zhu, 2019: Interdecadal change in the relationship between South China spring rainfall and preceding-summer warm pool ocean heat content. *J. Trop. Meteor.*, **25**, 462–470, https://doi.org/10.16555/j.1006-8775.2019.04.004.

Watanabe, M., 2004: Asian jet waveguide and a downstream extension of the North Atlantic Oscillation. *J. Climate*, **17**, 4674–4691, https://doi.org/10.1175/JCLI-3228.1.

Wei, F., 2007: *Modern Climate Statistical Diagnosis and Prediction Technology* (in Chinese). 2nd ed. China Meteorological Press, 296 pp.

Wu, H., S. Yang, and X. Jiang, 2015: Anomalous onset date of the first rainy season in South China and its relationship with the variation of the atmospheric circulation and SST (in Chinese). *Acta Meteor. Sin.*, **73**, 319–330.

Wu, J., and X.-J. Gao, 2013: A gridded daily observation dataset over China region and comparison with the other datasets (in Chinese). *Chin. J. Geophys.*, **56**, 1102–1111, https://doi.org/10.1007/10.6038/cjg20130406.

——, J. Li, Z. Zhu, and P.-C. Hsu, 2023: Factors determining the subseasonal prediction skill of summer extreme rainfall over southern China. *Climate Dyn.*, **60**, 443–460, https://doi.org/10.1007/s00382-022-06326-w.

Wu, X., and J. Mao, 2016: Interdecadal modulation of ENSO-related spring rainfall over South China by the Pacific decadal oscillation. *Climate Dyn.*, **47**, 3203–3220, https://doi.org/10.1007/s00382-016-3021-y.

Wu, Z., X. Li, Y. Li, and Y. Li, 2016: Potential influence of Arctic sea ice to the interannual variations of East Asian spring precipitation. *J. Climate*, **29**, 2797–2813, https://doi.org/10.1175/JCLI-D-15-0128.1.

Brought to you by INSTITUTE OF ATMOSPHERIC PHYSICS, CAS | Unauthenticated | Downloaded 07/13/23 02:29 PM UTC

Xi, J., L. Zhou, R. Murtugudde, and L. Jiang, 2015: Impacts of intraseasonal SST anomalies on precipitation during Indian summer monsoon. *J. Climate*, **28**, 4561–4575, https://doi.org/10.1175/JCLI-D-14-00096.1.

Xin, X., R. Yu, T. Zhou, and B. Wang, 2006: Drought in late spring of South China in recent decades. *J. Climate*, **19**, 3197–3206, https://doi.org/10.1175/JCLI3794.1.

Yang, F. L., and K.-M. Lau, 2004: Trend and variability of China precipitation in spring and summer: Linkage to sea-surface temperatures. *Int. J. Climatol.*, **24**, 1625–1644, https://doi.org/10.1002/joc.1094.

Yang, Y., Z. Zhu, X. Shen, L. Jiang, and T. Li, 2023: The influences of Atlantic sea surface temperature anomalies on the ENSO-independent interannual variability of East Asian summer monsoon rainfall. *J. Climate*, **36**, 677–692, https://doi.org/10.1175/JCLI-D-22-0061.1.

Yao, S., Q. Tong, T. Li, and K. Gong, 2020: The 10–30-day oscillation of winter rainfall in southern China and its relationship with circulation patterns in different latitudes. *Int. J. Climatol.*, **40**, 3268–3280, https://doi.org/10.1002/joc.6396.

You, Y., and X. Jia, 2018: Interannual variations and prediction of spring precipitation over China. *J. Climate*, **31**, 655–670, https://doi.org/10.1175/JCLI-D-17-0233.1.

Yuan, C., J. Liu, J.-J. Luo, and Z. Guan, 2019: Influences of tropical Indian and Pacific Oceans on the interannual variations of precipitation in the early and late rainy seasons in South China. *J. Climate*, **32**, 3681–3694, https://doi.org/10.1175/JCLI-D-18-0588.1.

Zeng, Z., and J. Sun, 2022: Decadal change of extreme consecutive dry days in spring over the middle and lower reaches of the Yangtze River around the early 2000s: The synergistic effect of mega-El Niño/Southern Oscillation, Atlantic Multidecadal Oscillation, and Arctic sea ice. *Atmos. Res.*, **266**, 105936, https://doi.org/10.1016/j.atmosres.2021.105936.

——, and ——, 2023: Influence of different configurations of western North Pacific anticyclone and Siberian high on spring climate over China. *Int. J. Climatol.*, **43**, 2699–2718, https://doi.org/10.1002/joc.7997

Zhang, L., P. Lin, Z. Xiong, and H. Wu, 2011: Impact of the Madden–Julian Oscillation on pre-flood season precipitation in South China (in Chinese). *Chin. J. Atmos. Sci.*, **35**, 560–570, https://doi.org/10.3878/j.issn.1006-9895.2011.03.15.

Zhang, M., and J. Sun, 2021: Impact of October snow cover in central Siberia on the following spring extreme precipitation frequency in southern China. *Front. Earth Sci.*, **9**, 785601, https://doi.org/10.3389/feart.2021.785601.

——, ——, and Y. Gao, 2022: Possible influence and predictive value of preceding winter sea ice anomalies in the Davis Strait-Baffin Bay for spring extreme precipitation frequency in eastern China (in Chinese). *Earth Sci. Front.*, **29**, 401–409.

Zheng, B., D. Gu, A. Lin, D. Peng, C. Li, and Y. Huang, 2022: Phase determination of persistent heavy rainfall related to 10–30-day intraseasonal oscillation over southeastern China. *Theor. Appl. Climatol.*, **147**, 1685–1695, https://doi.org/10.1007/s00704-021-03902-8.

Zhu, Z., T. Li, and J. He, 2014: Out-of-phase relationship between boreal spring and summer decadal rainfall changes in southern China. *J. Climate*, **27**, 1083–1099, https://doi.org/10.1175/JCLI-D-13-00180.1.

——, R. Lu, S. Fu, and H. Chen, 2023: Alternation of the atmospheric teleconnections associated with the Northeast China spring rainfall during a recent 60-year period. *Adv. Atmos. Sci.*, **40**, 168–176, https://doi.org/10.1007/s00376-022-2024-3.

Brought to you by INSTITUTE OF ATMOSPHERIC PHYSICS, CAS | Unauthenticated | Downloaded 07/13/23 02:29 PM UTC